TU Delft

Delft University of Technology

Benchmarking of Aerodynamic Models for Isolated Propellers Operating at Positive and Negative Thrust

Goyal, J.; Sinnige, T.; Avallone, F.; Ferreira, Carlos

DOI
10.2514/1.J064093

Publication date
2024

Document Version
Final published version

Published in
AIAA Journal: devoted to aerospace research and development

Citation (APA)
Goyal, J., Sinnige, T., Avallone, F., & Ferreira, C. (2024). Benchmarking of Aerodynamic Models for Isolated Propellers Operating at Positive and Negative Thrust. *AIAA Journal: devoted to aerospace research and development*, *62*(10), 3758-3775. https://doi.org/10.2514/1.J064093

Important note
To cite this publication, please use the final published version (if applicable).
Please check the document version above.

Copyright
Other than for strictly personal use, it is not permitted to download, forward or distribute the text or part of it, without the consent of the author(s) and/or copyright holder(s), unless the work is under an open content license such as Creative Commons.

Takedown policy
Please contact us and provide details if you believe this document breaches copyrights.
We will remove access to the work immediately and investigate your claim.

This work is downloaded from Delft University of Technology.
For technical reasons the number of authors shown on this cover page is limited to a maximum of 10.

Green Open Access added to TU Delft Institutional Repository

'You share, we take care!' - Taverne project

https://www.openaccess.nl/en/you-share-we-take-care

Otherwise as indicated in the copyright section: the publisher is the copyright holder of this work and the author uses the Dutch legislation to make this work public.

AIAA JOURNAL
Vol. 62, No. 10, October 2024

Benchmarking of Aerodynamic Models for Isolated Propellers Operating at Positive and Negative Thrust

Jatinder Goyal* and Tomas Sinnige†
Delft University of Technology, 2629 HS Delft, The Netherlands
Francesco Avallone‡
Polytechnic University of Turin, 10129 Turin, Italy
and
Carlos Ferreira§
Delft University of Technology, 2629 HS Delft, The Netherlands

https://doi.org/10.2514/1.J064093

Operating a conventional propeller at negative thrust results in the operation of positively cambered blade sections at negative angles of attack, leading to flow separation. Consequently, accurately simulating the aerodynamics of propellers operating at negative thrust poses a greater challenge than at positive thrust. This study offers a comprehensive assessment of the aerodynamic modeling capabilities of numerical methods, spanning low to high fidelity, for computing propeller performance across both positive and negative thrust regimes. Low-fidelity methods, namely, blade-element momentum and lifting line theories, effectively predict propeller performance trends at positive thrust. However, they fail to capture trends at negative thrust beyond the maximum power output point due to the neglect of three-dimensional flow effects. Both steady and unsteady Reynolds-averaged Navier–Stokes (RANS) simulations with $y^+ < 1$ perform well across both positive and negative thrust conditions, with errors below 2% for both thrust and power magnitudes near the maximum power output point. Lattice-Boltzmann very-large-eddy simulations (LB-VLESs) with $y^+ \leq 10$ exhibit excellent agreement with experimental data with less than 1% error near the maximum power output point but with significant computational costs. Conversely, LB-VLESs with $y^+ \geq 15$ offer a more economical approach to capture general trends with the computational cost of the same order as unsteady RANS. However, wall models introduce errors in modeling flow separation, leading to a 16% overestimation of power magnitude near the maximum power output point. The results highlight the necessity of using tools with increased fidelity levels when considering propeller operation at negative thrust compared to the conventional positive thrust regime.

Downloaded by Technische Universiteit Delft on October 7, 2024 | http://arc.aiaa.org | DOI: 10.2514/1.J064093

Nomenclature

a	=	axial induction, V_a/V_∞
C_f	=	skin-friction coefficient, τ_w/q_∞
C_n	=	normal-force coefficient, $\int_0^1 C_{p_s}\,\mathrm{d}\zeta/c$
C_P	=	propeller power coefficient, $P/\rho_\infty n^3 D^5$
C_{p_s}	=	static pressure coefficient, $(p-p_\infty)/q_{\text{eff}}$
C_{p_t}	=	total pressure coefficient, $(p_t-p_{t_\infty})/q_\infty$
C_T	=	propeller thrust coefficient, $T/\rho_\infty n^2 D^4$
c	=	section chord, m
c_d	=	sectional drag coefficient, $D'/q_\infty c$
c_l	=	sectional lift coefficient, $L'/q_\infty c$
c_p	=	sectional power coefficient, $P'/\rho_\infty n^3 D^4$
c_q	=	sectional torque coefficient, $Q'/\rho_\infty n^2 D^4$
c_t	=	sectional thrust coefficient, $T'/\rho_\infty n^2 D^3$
D	=	propeller diameter, m
D'	=	sectional drag force, N/m
h_i	=	average cell size of grid i, m
J	=	propeller advance ratio, V_∞/nD
L'	=	sectional lift force, N/m
M	=	Mach number
n	=	propeller rotation speed, Hz
P	=	propeller power, W
p	=	static pressure, Pa
p_t	=	total pressure, Pa
Q	=	torque, N·m
q	=	dynamic pressure, $p_\infty(1+((\gamma-1)/2)M^2)^{\gamma/(\gamma-1)}-p_\infty$, Pa
R	=	propeller radius, m
R_x	=	slipstream radius at x, m
r	=	radial coordinate, m
T	=	propeller thrust, N
t	=	section thickness, m
U_ϕ	=	estimated discretization uncertainty
V	=	velocity, m/s
x	=	axial coordinate, m
y^+	=	dimensionless wall distance
α	=	angle of attack, deg
$\beta_{0.7R}$	=	blade pitch angle at 70% of the radius, deg
Δt	=	time step, s
δP	=	pressure jump over given annulus, N/m^2
δr	=	radial width of given annulus, m
δT	=	thrust over given annulus, N
ζ	=	chordwise coordinate, m
η_{eh}	=	energy-harvesting efficiency, $-8P/\rho_\infty \pi D^2 V_\infty^3$
η_p	=	propeller efficiency, TV_∞/P
η_t	=	turbine efficiency, P/TV_∞
ρ	=	air density, kg/m^3
τ_w	=	wall shear stress, Pa
$\boldsymbol{\omega}_t^*$	=	nondimensional in-plane vorticity, $\boldsymbol{\omega}_t D/V_\infty$
$\boldsymbol{\omega}_t$	=	in-plane vorticity, 1/s

Subscripts

a	=	axial

Received 23 February 2024; revision received 7 May 2024; accepted for publication 13 May 2024; published online Open Access 23 July 2024. Copyright © 2024 by J. Goyal, T. Sinnige, F. Avallone, and C. Ferreira. Published by the American Institute of Aeronautics and Astronautics, Inc., with permission. All requests for copying and permission to reprint should be submitted to CCC at www.copyright.com; employ the eISSN 1533-385X to initiate your request. See also AIAA Rights and Permissions www.aiaa.org/randp.

*Ph.D. Candidate, Wind Energy Section, Faculty of Aerospace Engineering; j.goyal@tudelft.nl.
†Assistant Professor, Flight Performance and Propulsion Section, Faculty of Aerospace Engineering; t.sinnige@tudelft.nl.
‡Full Professor, Department of Mechanical and Aerospace Engineering; francesco.avallone@polito.it.
§Full Professor, Wind Energy Section, Faculty of Aerospace Engineering, Kluyverweg 1; c.j.simaoferreira@tudelft.nl.

eff = combination of axial and rotational components
∞ = freestream

Superscript

′ = per unit span

I. Introduction

THE emergence of electric aviation has sparked a renewed interest in propellers. Propellers can be easily combined with electric motors to achieve new configurations for which increased interaction between the propulsion system and wing can enhance the overall aerodynamic performance of the aircraft [1–3]. One additional benefit of combining propellers with electric propulsion is that propellers can be operated at negative thrust settings that can be beneficial for achieving steeper descent, reduced landing run, better maneuverability [4,5], reduced community noise [6], and regeneration of energy [7,8].

A propeller can be used to produce negative thrust by adjusting the blade pitch and rotational speed so that the angles of attack at the blade sections become such that negative lift is produced (see Fig. 1). The generation of negative thrust is accompanied by a negative torque, which can be converted to electrical energy to power the electrical systems onboard. Propeller design optimization efforts by Pipistrel for a small electric trainer aircraft led to energy savings of 19%, showing the potential of the concept [7]. Moreover, this concept has been successfully implemented for marine applications in the Opal ship [9].

Investigations of different conventional propellers in the negative thrust regime have reported energy-harvesting efficiency values of about 10% without any optimization for this mode [8,10,11]. The low energy-harvesting efficiency values for conventional propellers result from the contrasting nature of positive and negative thrust operations. A conventional propeller optimized for the positive thrust regime has positively cambered blade sections. Using such conventional propellers at negative thrust conditions requires the operation of these positively cambered blade sections at negative angles of attack (see Fig. 1b). Therefore, the propeller blades are prone to flow separation when operating at negative thrust conditions, resulting in poor aerodynamic performance [8,11–13]. An alternative approach to mitigate this issue is to invert the blade pitch and rotate the propeller in the opposite direction. However, this approach presents several challenges, including inverted blade twist and potentially requiring complex control mechanisms. Therefore, such an approach is deemed impractical in real-flight conditions and is not considered in this study.

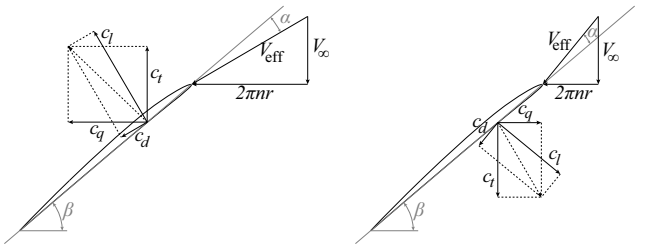

a) Positive thrust mode **b) Negative thrust mode**

Fig. 1 Velocity triangles at a fixed-pitch propeller blade section in propulsive and energy-harvesting mode. Reprinted with permission from Tomas Sinnige. Source: [8].

Given the complex aerodynamics associated with negative thrust conditions, the tools/models capable of accurate performance predictions in positive thrust conditions may not be reliable anymore in negative thrust conditions. Therefore, it is critical to benchmark the capabilities of different aerodynamic models in the negative thrust regime compared to the positive thrust regime.

This paper addresses this need by systematically evaluating numerical methods of varying fidelity against experimental data. The spectrum of fidelity encompasses low-fidelity tools like blade element momentum (BEM) and lifting line (LL) theories, midfidelity through steady Reynolds-averaged Navier–Stokes (SRANS), and high-fidelity simulations involving unsteady RANS (URANS) and lattice-Boltzmann (LB) very-large-eddy simulations (VLESs). Through this comprehensive investigation, this paper aims to provide valuable insights into the performance and limitations of these methods in both positive and negative thrust conditions. This information will assist the research community in selecting the most suitable numerical method based on their specific research objectives and available computational resources.

II. Propeller Geometry and Reference Experimental Setup

The propeller used in this study is the TUD-XPROP, a scaled version of a propeller for a previous-generation regional turboprop aircraft. The propeller has a diameter of 0.4064 m and a hub diameter of 0.092 m. The nacelle of the propeller extended up to approximately 1.6 D downstream. Originally, the propeller had six blades; however, only three blades were used in the reference experiment due to the limitations of the power dissipation system when operating at negative thrust [11]. Therefore, the three-bladed variant of the propeller has been used in this study. The propeller can be seen in Fig. 2a, along with its geometry parameters in Fig. 2b.

To validate numerical methods, comparisons are made with experimental load cell data, 5-hole pressure probe data, and phase-locked particle image velocimetry (PIV) data from Nederlof et al. [11] at a pitch setting of 15° at $0.7R$ ($\beta_{0.7R} = 15°$). The experiments were conducted at a freestream Mach number of 0.09, with the helicoidal tip Mach number ranging from 0.21 to 0.51. The Mach numbers at the

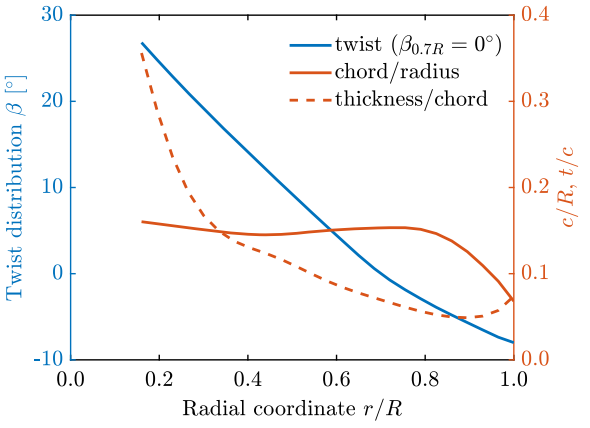

a) Isolated propeller with three blades installed on a sting **b) Propeller blade geometry**

Fig. 2 Propeller setup in the wind tunnel and geometry.

Downloaded by Technische Universiteit Delft on October 7, 2024 | http://arc.aiaa.org | DOI: 10.2514/1.J064093

Downloaded by Technische Universiteit Delft on October 7, 2024 | http://arc.aiaa.org | DOI: 10.2514/1.J064093

propeller blades are considered representative of subsonic conditions. As the TUD-XPROP is a scaled-down model, the Reynolds number, based on the chord of the blade sections in experiments, is an order of magnitude lower than in full-scale flights. Operating the propeller at these lower Reynolds numbers in the experiments led to an increased susceptibility to flow separation and the presence of separation bubbles on the propeller blades. Consequently, matching numerical results with experimental data at these lower Reynolds numbers is more challenging than full-scale flight conditions.

The experimental data used in the present paper were corrected for wind-tunnel boundary interference. Three different corrections were applied to correct the freestream velocity based on the study of Barlow et al. [14]: 1) solid blockage due to the nacelle, 2) solid and wake blockage due to the sting (support structure), and 3) propeller slipstream blockage. Subsequently, response models for C_T and C_P as a function of J were determined based on the corrected data using polynomial fits. The order of the polynomial fits was determined by assessing the variation of root mean square error and t-statistics with the order of the polynomial, resulting in a fourth-order polynomial fit for C_T versus J and a third-order polynomial fit for C_P versus J. The uncertainties of the response models were based on 95% prediction bounds. The results for other parameters (η_p, η_t, and η_{eh}) were calculated from the results obtained from the response models for C_T and C_P.

III. Numerical Methods

In this study, methods ranging from low-fidelity to high-fidelity have been used to simulate propeller performance in positive and negative thrust regimes, as listed in Fig. 3. These methods and the computational setups are briefly described in this section.

A. Blade-Element-Momentum Theory

A classic BEM model was implemented based on Rwigema [15] and Burton et al. [16]. The blade section properties (lift and drag polar data) were calculated using RFOIL [17], which is a modification of the well-known two-dimensional-panel (2D-panel) method XFOIL [18]. RFOIL was selected for its better lift and drag coefficient prediction in the post-stall region [19]. Moreover, the quasi-three-dimensional (quasi-3D) model available in RFOIL was utilized to account for the influence of Coriolis and centrifugal forces on the boundary-layer characteristics of rotating airfoils [20,21]. The source code of the BEM model used in this study can be found on 4TU.ResearchData repository [22].

The BEM calculations used 50 radial stations with cosine distribution along the blade span to achieve higher resolution in the root and tip regions of the blade, where the gradients in loading are highest. To account for compressibility and Reynolds number effects, polar data was collected at different Mach and Reynolds numbers at 24 radial stations using RFOIL. Subsequently, the data was interpolated to local Mach and Reynolds numbers based on the local effective velocity and chord of the airfoil sections along the blade span. This interpolation occurred in two steps. Firstly, the polar data was interpolated using Delaunay triangulation of the sample points. In this step, the polar data was obtained for the given radial location at a given angle of attack and the local Reynolds number for all the input Mach numbers. In the subsequent step, the acquired polar data was linearly interpolated to obtain the values at the specified local effective Mach number. To account for hub and tip loss, Prandtl tip correction [23] was implemented. Additionally, Glauert's correction [16] was implemented for highly loaded propellers in the negative thrust regime.

B. Lifting Line Theory

This research used the semi-free-wake lifting-line (LL) theory as described by Katz and Plotkin [24]. Although a free-wake lifting-line theory would provide higher accuracy, its substantial computational resource requirements make it impractical for design optimization studies. The same polar data and interpolation scheme were used for the lifting line as for BEM theory in the preceding section. Also, the compressibility and Reynolds number effects were taken into account in the same manner as in the BEM theory.

Increasing Fidelity →

BEM LL SRANS URANS LB-VLES

Fig. 3 Numerical tools considered in this study.

The LL calculations were performed using 50 radial stations uniformly distributed along the blade span (unlike BEM theory) to avoid numerical instability caused by small elements at the root and tip. The pitch of the wake was defined based on the solution as per the so-called semi-free-wake approach. An initial helical wake was defined with an arbitrary pitch based on the initial guess of the average axial induction (a) at the rotor. Based on this wake, the converged circulation distribution (change in circulation $\leq 10^{-6}$ per section) and induction were calculated at the propeller blades. The pitch of the helical wake was redefined based on this converged average axial induction at the rotor until the change in the newly calculated average axial induction was within the tolerance level (10^{-3}).

To account for the contraction of the helical wake, Eq. (1) derived by Veldhuis [25] was used. Though this wake model does not account for vortex roll-up, it does account for the influence of the axial velocity increment and contraction within the slipstream.

$$\frac{r_x}{r} = \sqrt{\frac{1+a}{1+a\left(1+\frac{x}{\sqrt{r^2+x^2}}\right)}} \tag{1}$$

where r_x is the contracted radius of the annulus [m] at an axial distance of x downstream of the propeller [m], r is the radius of the annulus at the propeller disk [m], and a is the average axial induction of the given annulus at the rotor disk.

C. Steady RANS Simulations

1. Solver Description and Numerical Setup

The RANS equations for compressible flow were solved using ANSYS® Fluent 2019 R3 [26], which is a commercial, unstructured, finite-volume, cell-centered solver. As only uniform inflow conditions have been studied in this paper, these simulations were solved for a single-blade wedge domain in a steady manner using a multireference-frame approach. The computational domain used for these simulations can be seen in Fig. 4. It was made sure that the boundaries of the domains were sufficiently far away to keep the influence of boundary

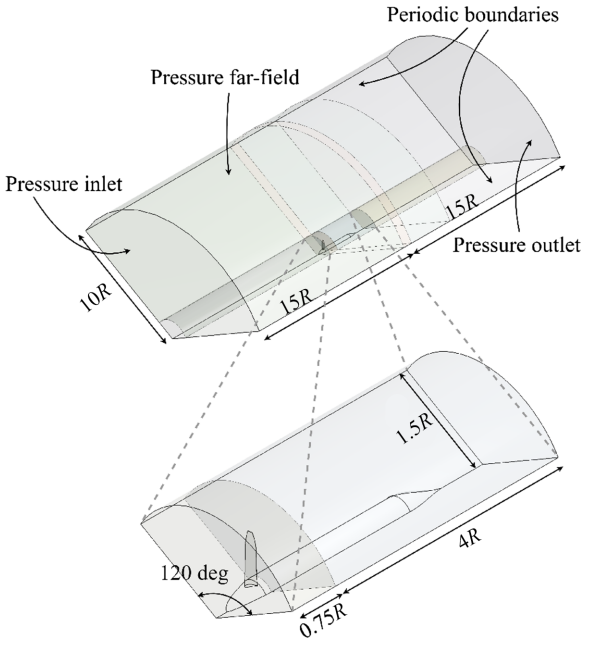

Fig. 4 Numerical domain and boundary conditions for steady RANS simulations.

Downloaded by Technische Universiteit Delft on October 7, 2024 | http://arc.aiaa.org | DOI: 10.2514/1.J064093

conditions on the flow properties near the propeller blade minimum [8,27,28]. The height of the block of the domain in the vicinity of the propeller blade was chosen to be $1.5R$ to allow for wake expansion in negative thrust conditions and was refined to capture the propeller slipstream. The height of the domain was chosen to be $10R$ with a wedge angle of 120°.

Following the CFD setup of previous research efforts for similar problems [8,27,28], total-pressure inlet, pressure outlet, and pressure far-field boundary conditions were used in combination with a conformal periodic boundary condition for the side boundaries to avoid interpolation errors. The propeller blade and spinner were modeled as no-slip stationary walls in the moving reference frame, and the nacelle was modeled as a no-slip stationary wall in the absolute reference frame. The air density was calculated using the ideal gas assumption, and the dynamic viscosity was computed using Sutherland's law. The turbulence modeling was based on the Spalart–Allmaras method with a modification proposed by Dacles-Mariani et al. [29,30].

ANSYS Meshing was used for grid generation. Adjacent to no-slip wall regions, a triangular wall mesh and layers of semistructured prismatic and tetrahedral elements were used. On the other hand, an unstructured hexagonal mesh was created in the far slipstream and upstream of the propeller to reduce the total number of elements. The first-layer thickness of inflation layers was tuned to keep the $y^+ \leq 1$ as per the requirement of the Spalart–Allmaras turbulence model. The grid density in the whole domain was controlled by the wall refinement of no-slip walls and the volume refinement of the domains. The grid density was kept similar over the propeller blade and nacelle, i.e., the zoomed part of the domain shown in the bottom part of Fig. 4. Upstream and downstream of the blade and nacelle, the grid density was reduced to optimize the computational cost.

2. *Grid Convergence Study*

The grid was refined systematically for the grid convergence study, except for the inflation layer, as per the recommendation of starting the grid convergence study from the edge of the wall layer out by Roache [31]. Following the methodology of Stokkermans et al. [27], the least-squares version of the grid convergence index proposed by Eça and Hoekstra [32] was used to estimate discretization error. Table 1 lists the grid size and refinement ratios h_i/h_1 for the studied configurations, where h_i is the average cell size of the grid i and h_1 represents the average cell size of the finest grid. Four different grids were used for the grid convergence study, where grid 4 is the coarsest, and grid 1 is the finest.

The systematic grid convergence analysis was performed based on the integrated thrust and power coefficients for two operating conditions. Additionally, a qualitative assessment was made of the convergence in terms of the radial distributions of thrust and power along the blade span. The two conditions were chosen as the most challenging ones to reproduce numerically. The first condition is a positive thrust condition with a moderate thrust at $J = 0.61$ with $\beta_{0.7R} = 15°$. The given pitch angle is not optimal for propulsive operation and leads to separation near the trailing edge [12]. Therefore, if the grid results are converged for such an operating condition, it can be safely assumed to be converged for other positive thrust conditions with fully attached flow. However, the grid convergence in the positive thrust regime does not ensure the convergence in the negative thrust regime because of significant flow separation around the blades in the latter condition [8,12]. Therefore, the second condition is the negative thrust condition at $J = 1.10$ with $\beta_{0.7R} = 15°$, close to the maximum power output point.

Table 1 Grid size of the SRANS simulations

Grid	No. of cells	h_i/h_1
4	2,909,433	1.87
3	6,097,112	1.46
2	9,620,832	1.26
1	19,130,159	1.00

Table 2 Grid convergence study of SRANS simulations

	$J = 0.61$		$J = 1.10$	
Grid	C_T	C_P	C_T	C_P
4	0.03917	0.03785	−0.12713	−0.05458
3	0.03907	0.03776	−0.12660	−0.05420
2	0.03909	0.03778	−0.12724	−0.05480
1	0.03915	0.03779	−0.12803	−0.05537
Discretization error $\lvert U_\phi \rvert$, % (Based on grid 2)	**0.78**	**0.74**	**3.37**	**6.40**

The results from the grid convergence study are given in Table 2, where U_ϕ represents the estimated discretization error based on the solution of the chosen grid (grid 2). Due to the onset of separation near the tip of the blade (discussed later in Sec. IV.B), an oscillatory convergence was observed for both operating points. Due to the oscillatory convergence, the discretization error was determined using $U_\phi = 3\Delta_M$, where Δ_M represents the maximum difference between all the available solutions [32]. The propulsive condition ($J = 0.61$) has a maximum estimated discretization error of less than 1% for both C_T and C_P. However, the maximum estimated discretization error for the negative thrust condition ($J = 1.10$) is 3.37% and 6.40% for C_T and C_P, respectively. The increased discretization error results from significant flow separation on the propeller blades.

To further check the discrepancies between solutions obtained for different grids, radial distributions of thrust and power are compared in Fig. 5 for the operating point corresponding to the maximum uncertainty, i.e., $J = 1.10$. It can be observed that except, for some minor differences in the outer region of the blade due to the onset of separation, the solutions for all the grids are in reasonable agreement. Assuming grid 1 (the finest grid) as the reference, grid 2 provides a better match of radial distributions of both thrust and power compared to the other grids. Therefore, grid 2 was determined to be the most suitable in terms of the tradeoff between computational cost and solution refinement and, therefore, was used to generate the results discussed in the rest of the paper.

D. Unsteady RANS Simulations

The setup for unsteady RANS (URANS) simulations was similar to the setup used for SRANS. Assuming the URANS solution will behave in a similar way as SRANS data, the grid 2 used for SRANS simulations was copied and rotated to generate the remaining two blades of the propeller geometry, resulting in a cylindrical domain. The sliding mesh approach was used to solve the URANS equations with a time step equivalent to a 2° rotation for all the advance ratios considered in this study. The time step was chosen based on the recommendation by Stokkermans et al. [27]. The second-order backward Euler scheme was used with the implicit formulation for the time-stepping. The URANS simulation was initialized with the converged solution from the SRANS solution of the cylindrical domain. The simulation was run for two rotations, from which the last rotation was used for the analysis. It was ensured that the results from the last rotation were converged by monitoring the integrated forces and checking the variation in blade loading over the rotation.

E. Lattice-Boltzmann Very-Large-Eddy Simulations

The LB-VLESs represent the highest-fidelity numerical approach employed in this paper. For a comprehensive understanding of the lattice-Boltzmann method (LBM), readers can refer to the detailed descriptions available in Succi [33] and Shan et al. [34]. The LB-VLES equations were solved using SIMULIA® PowerFLOW 6-2021-R6, a commercially available solver. The LB-VLES solver implemented in PowerFLOW uses a wall model approach. However, as shown by Romani and associates [35], in order to well predict boundary-layer separation and start resolving turbulence features, near-wall grid refinement is needed with $y^+ \leq 10$.

Unlike traditional RANS simulations, where stretched cells can be used to achieve low y^+ values, the LB-VLES solver implemented in

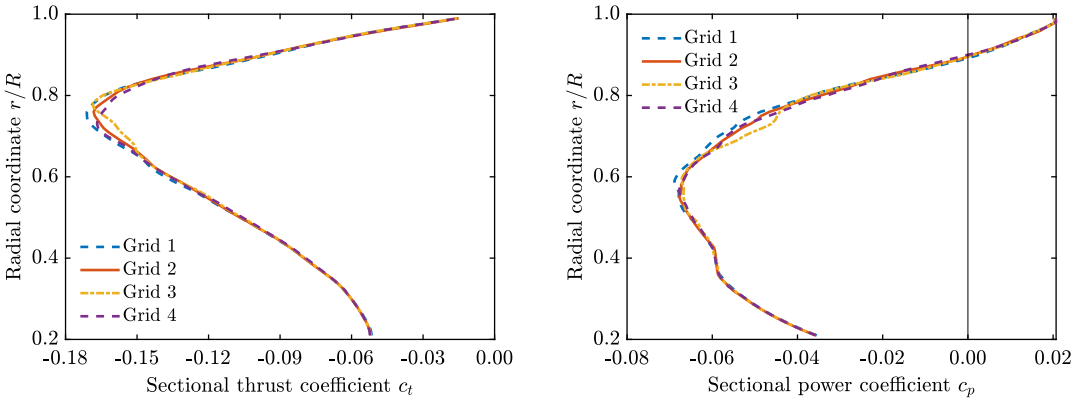

a) Thrust distribution along the propeller blade span **b) Power distribution along the propeller blade span**

Fig. 5 Effect of grid refinement on the thrust and power distribution along the propeller blade for the negative thrust condition ($J = 1.10$).

Downloaded by Technische Universiteit Delft on October 7, 2024 | http://arc.aiaa.org | DOI: 10.2514/1.J064093

PowerFLOW requires cells with a strict aspect ratio of 1 and a Courant number below 1. These requirements result in a significant computational cost increase when attempting to reach $y^+ \leq 10$ over the propeller blade surface. This cost increase is attributed to the need for both an increase in mesh size (number of cells) and a decrease in the time step with the decrease in y^+ at the blade surface. Consequently, though LB-VLESs with $y^+ \leq 10$ can be instrumental in obtaining the detailed flow features around the propeller blades and understanding the propeller aerodynamics and aeroacoustics (especially in the presence of flow separation), this great detail comes at an equally great computational cost.

Therefore, most practical studies use $y^+ \geq 15$ to reduce the computational cost. However, it is essential to remember that higher y^+ values can delay the transition to resolved turbulence, potentially leading to inaccuracies in predicting features like flow separation and reattachment. Considering these advantages and drawbacks, this study employed two types of LB-VLESs:

1) LB-VLESs$_{y^+\geq 15}$: These LB-VLESs were run with $y^+ \geq 15$. The simulations ran for ten propeller rotations, with the final eight used for analysis. Note that only four revolutions were needed to achieve the converged aerodynamic solution; however, the simulation was run longer due to the interest in aeroacoustics (not discussed in this paper).

2) LB-VLESs$_{y^+\leq 10}$: These LB-VLESs were run with $y^+ \leq 10$. Due to the extreme computational requirements of LB-VLESs$_{y^+\leq 10}$, only two conditions were simulated using this strategy: $J = 0.60$ and 1.10. The first condition corresponds to the positive thrust condition, and the second condition corresponds to the negative thrust condition. These simulations were initialized using the solution of LB-VLESs$_{y^+\geq 15}$. The LB-VLESs$_{y^+\leq 10}$ were run in total for four propeller rotations, out of which the last three were used for the analysis. Only two revolutions were required to obtain the converged aerodynamic solution; however, the simulation was run longer due to the interest in aeroacoustics (not discussed in this paper).

1. Solver Description and Numerical Setup

The computational domain was a cube with a domain size of $128D$ in all three directions (see Fig. 6a). Note that such a large domain size was motivated by an interest in aeroacoustics rather than in aerodynamics. The computational domain was discretized using a Cartesian mesh, employing 19 discrete velocities in three dimensions (D3Q19), including a third-order truncation of the Chapman–Enskog expansion. An explicit time integration approach was applied to solve the equations with a Courant–Friedrichs–Lewy (CFL) number of 1 to maintain numerical stability. The particle distribution within the domain was determined using a collision term based on a unique Galilean invariant [36], and the equilibrium distribution followed the Maxwell–Boltzmann distribution [37]. PowerFLOW utilizes a very-large-eddy simulation (VLES) model to account for the effects of subgrid unresolved turbulence scales. This model relies on the $k-\epsilon$ renormalization equations [38] to predict the turbulent relaxation time, a crucial parameter in turbulence modeling.

The domain's boundaries were specified as a velocity inlet, a pressure outlet, and slip walls. The large domain size ensured a uniform total pressure profile at the inlet and minimized the influence of boundary conditions on the simulation results. No-slip conditions were applied to the propeller blades, spinner, and nacelle. The treatment of no-slip boundary conditions on walls in PowerFLOW involves an approximation using a pressure-gradient extended wall model [39,40]. This model extends the generalized law-of-the-wall model [41] to consider the impact of pressure gradients on boundary-layer development.

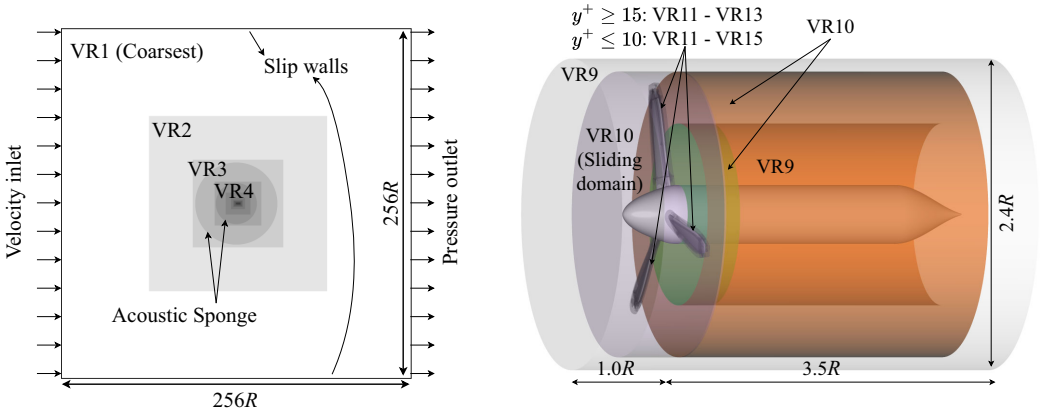

a) Full computational domain **b) Zoomed view of domain showing the distribution of VR regions near the propeller**

Fig. 6 Computational domain and boundary conditions along with the VR regions for LB-VLESs.

Downloaded by Technische Universiteit Delft on October 7, 2024 | http://arc.aiaa.org | DOI: 10.2514/1.J064093

For the sliding mesh, a volume of revolution was defined around the propeller blades and spinner (see Fig. 6b). In the radial direction, a clearance of $0.1R$ was defined between the blade tip and the outer edge of the rotating domain. Similarly, in the axial direction, a clearance of $0.05R$ was defined between the spinner edge and the edge of the rotating domain.

In total, 13 variable-resolution (VR) regions were employed for LB-VLES$s_{y^+\geq 15}$, based on the work of Avallone et al. [42]. The LB-VLES$s_{y^+\leq 10}$ included two additional VR regions within VR13. Therefore, only the voxels surrounding the propeller blades were modified in LB-VLES$s_{y^+\leq 10}$. The cell volume changes by a factor of 8 between different VR regions. The finest three VR regions (VR13-11) in LB-VLES$s_{y^+\geq 15}$ are marked in Fig. 6b. VR10 was used in the sliding domain and downstream up to a distance of $0.5R$ from the propeller. Further downstream, a hollow cylinder with VR10 resolution was used to capture the strong gradients associated with tip vortices. Finally, VR9 was used in a cylinder with a radius of $1.2R$ encompassing the propeller blades, spinner, and blade, extending $1R$ upstream and $3.5R$ downstream of the propeller.

Beyond the primary VR regions, VR regions 4–8 were required to ensure domain size sufficiency to minimize the impact of boundary conditions on the aerodynamic solution. Further, three additional VR regions (VR1-3) were used to minimize acoustic reflections, resulting in such a large domain size ($128D$). An acoustic sponge was also used between VR3 and VR4 to absorb any remaining acoustic reflections coming from the boundaries by exponentially varying the kinematic viscosity per unit temperature from 0.005 $m^2/(s \cdot K)$ at $15R$ up to 0.5 $m^2/(s \cdot K)$ at $30R$ as shown in Fig. 6a. The acoustic sponge started at a distance of $15R$ from the propeller center, ensuring minimal impact on the aerodynamic results.

It is important to note that, in PowerFLOW, the computational cost of cells within a coarser VR region decreases by a factor of 2^{N-1}, where N is the number of VR regions finer than the considered VR region. This means that despite expanding the domain to $128D$ compared to the conventional domain size of $15D$–$20D$ for aerodynamic simulations, the increase in the computational cost due to the additional VR regions (VR1-3) was negligible.

A detailed grid convergence study was conducted for LB-VLES$s_{y^+\geq 15}$. The details of the grid convergence study and further details of the setup can be found in the authors' previous work [43].

Table 3 List of operating conditions simulated using mid- and high-fidelity numerical methods

	$T > 0$		$T < 0$					
J	0.60	0.61	0.75	0.89	1.09	1.10	1.28	1.48
SRANS	✓	✓	✓	✓	✓	✓	✓	✓
URANS	✓	✓	✓	✓	✓	✓	✓	✓
LB-VLES$_{y^+\geq 15}$	✓	✓	✓	✓	✓	✓	✓	✓
LB-VLES$_{y^+\leq 10}$	✓					✓		

F. Overview of Operating Conditions

All the simulations in this paper have been carried out for a fixed pitch angle of 15° at $0.7R$ of the blade and a freestream Mach number of 0.09. These settings were chosen based on the available experimental data for validation purposes [11].

The low-fidelity tools BEM and LL were evaluated at numerous advance ratios ranging from $J = 0.55$ to 1.48 due to their lower computational cost. SRANS, URANS, and LB-VLES$s_{y^+\geq 15}$ were evaluated at eight advance ratios. Due to the considerably higher computational cost associated with LB-VLES$s_{y^+\leq 10}$, only two advance ratios ($J = 0.60, 1.10$) were simulated using this high-fidelity tool. Table 3 details the different advance ratios simulated using mid- and high-fidelity tools.

G. Comparison of Grid Specifications and Computational Costs

Tables 4 and 5 present a comprehensive overview of the distinctions in grid specifications, time step settings, and the resultant computational expenses across different numerical tools, categorized by positive thrust condition ($J = 0.60$) and negative thrust condition ($J = 1.10$), respectively. It is imperative to acknowledge that the CPU hours listed in Tables 4 and 5 offer a rough estimation of the computational cost associated with these methods. The actual computational expenses may vary depending on factors such as the number of CPUs utilized and the underlying CPU architecture.

For SRANS and URANS simulations, the grid remains consistent across different advance ratios. However, LB-VLESs require a new grid for each change in advance ratio. URANS simulations have precisely three times the number of cells as SRANS simulations, obtained by copying and rotating the grid from SRANS simulations to obtain the entire propeller geometry.

The CPU hours required for the SRANS simulations depend on the grid and the number of iterations needed to achieve convergence, which does not change significantly with the advance ratio. In this paper, the SRANS simulations were run for 10,000 iterations to obtain the converged aerodynamic solution, resulting in the computational cost of 780 and 800 h for $J = 0.60$ and 1.10, respectively. This cost is significantly higher (approximately 40,000–50,000 times) than the low-fidelity tools BEM and LL, with a computational cost of less than 1 minute.

Table 4 Grid specifications of mid- and high-fidelity numerical methods for the positive thrust condition ($J = 0.60$)

Method	y^+	No. of cells	Δt, s	Rotation per time step, °	Average CPU hours per revolution	Total CPU hours for converged aerodynamic solution	No. of iterations or revolutions required for converged aerodynamic solution
SRANS	<1	9,620,832	— —	— —	78 h per 1,000 iters	780	10,000 iters
URANS	<1	28,862,496	4.516e−05	2°	2,232	5,634	2 revs + initialization
LB-VLES$_{y^+\geq 15}$	≥15	62,314,804	1.654e−07	7.324e − 03°	1,572	6,288	4 revs
LB-VLES$_{y^+\leq 10}$	≤10	235,590,308	4.134e−08	1.831e − 03°	49,766	105,820	2 revs + initialization

Table 5 Grid specifications of mid- and high-fidelity numerical methods for the negative thrust condition ($J = 1.10$)

Method	y^+	No. of cells	Δt, s	Rotation per time step, °	Average CPU hours per revolution	Total CPU hours for converged aerodynamic solution	No. of iterations or revolutions required for converged aerodynamic solution
SRANS	<1	9,620,832	— —	— —	80 h per 1,000 iters	800	10,000 iters
URANS	<1	28,862,496	8.279e−05	2°	810	2,820	2 revs + initialization
LB-VLES$_{y^+\geq 15}$	≥15	62,029,252	1.732e−07	4.185e − 03°	2,461	9,844	4 revs
LB-VLES$_{y^+\leq 10}$	≤10	234,454,461	4.331e−08	1.046e − 03°	83,945	177,734	2 revs + initialization

Downloaded by Technische Universiteit Delft on October 7, 2024 | http://arc.aiaa.org | DOI: 10.2514/1.J064093

The URANS simulations were initialized using the SRANS solution of the entire propeller geometry obtained after 5000 iterations to reduce the total number of revolutions required to obtain the converged solution. The CPU hours per revolution for URANS simulations depend on the number of iterations required for each time step to reach convergence. Achieving convergence criteria of residuals lower than 1e−5 required 20 inner iterations for $J = 1.10$, while $J = 0.60$ required over 50 iterations, substantially increasing CPU hours per rotation for the latter condition.

The LB-VLESs$_{y^+\geq 15}$ have a time step of two orders of magnitude smaller than the URANS and almost three times as many cells. Nevertheless, for $J = 0.60$, LB-VLES$_{y^+\geq 15}$ exhibits lower computational costs per revolution (1572 h) than URANS simulation (2232 h), primarily due to the high number of inner iterations required for URANS. Conversely, at $J = 1.10$, the computational cost per revolution for LB-VLES$_{y^+\geq 15}$ (2461 h) is almost three times higher than URANS simulations (810 h). This disparity arises from the lower number of inner iterations required to meet the convergence criteria in the URANS simulation and a higher number of time steps per revolution in the LB-VLES$_{y^+\geq 15}$. The LB-VLESs$_{y^+\geq 15}$ needed to be run longer (4 revolutions) compared to the URANS simulations (two revolutions) to achieve convergence of the aerodynamic solution due to the lack of a good initialization for the former. This resulted in a higher total computational cost for LB-VLESs$_{y^+\geq 15}$ compared to URANS simulations, regardless of the advance ratios.

To reduce the total number of revolutions required to obtain the converged solution, the LB-VLESs$_{y^+\leq 10}$ were initialized using the solution of LB-VLESs$_{y^+\geq 15}$. As a result, only two revolutions were required to achieve the converged aerodynamic solution. In LB-VLESs$_{y^+\leq 10}$, the mesh size increases by almost a factor of 4, and the time step decreases precisely by a factor of 4 compared to LB-VLESs$_{y^+\geq 15}$. Theoretically, the computational cost (per revolution) of LB-VLESs$_{y^+\leq 10}$ should increase roughly by a factor of 16 compared to LB-VLESs$_{y^+\geq 15}$. However, the increase in computational cost per revolution surpasses the factor of 16 for both advance ratios due to the increase in simulation data saving time and due to the nonlinear scalability of the simulations with increasing CPUs. The increased computational cost for the $J = 1.10$ operating condition in both types of LB-VLESs is attributed to the lower rotation per time step compared to the $J = 0.60$ condition.

IV. Comparison of Numerical and Experimental Results

This section compares the results obtained from various numerical methods with the experimental data. Given the significance of integrated performance as a fundamental metric in design optimization studies, it is the first one presented in the analysis. The differences observed in integrated performance are explained by showing skin friction contours on the propeller surface and streamlines around distinct blade sections. Next, the total pressure coefficient in the propeller slipstream has been used as an additional parameter, which can be used as the baseline for blade loading comparison in the absence of blade loading distributions from the experiments. The section concludes with a comparison based on phase-locked in-plane vorticity within the propeller slipstream, deemed relevant for investigations of propeller–wing interactions.

A. Time-Averaged Integrated Performance

This section presents a comparative analysis of five distinct parameters as a function of advance ratio (J): thrust coefficient (C_T), power coefficient (C_P), energy-harvesting efficiency (η_{eh}), as well as propeller and turbine efficiency (η_p, η_t). The variation of these parameters with the advance ratio is plotted in Fig. 7, showing the predictions from different numerical tools compared to experimental results. Additionally, Tables 6 and 7 quantify the differences in the integrated

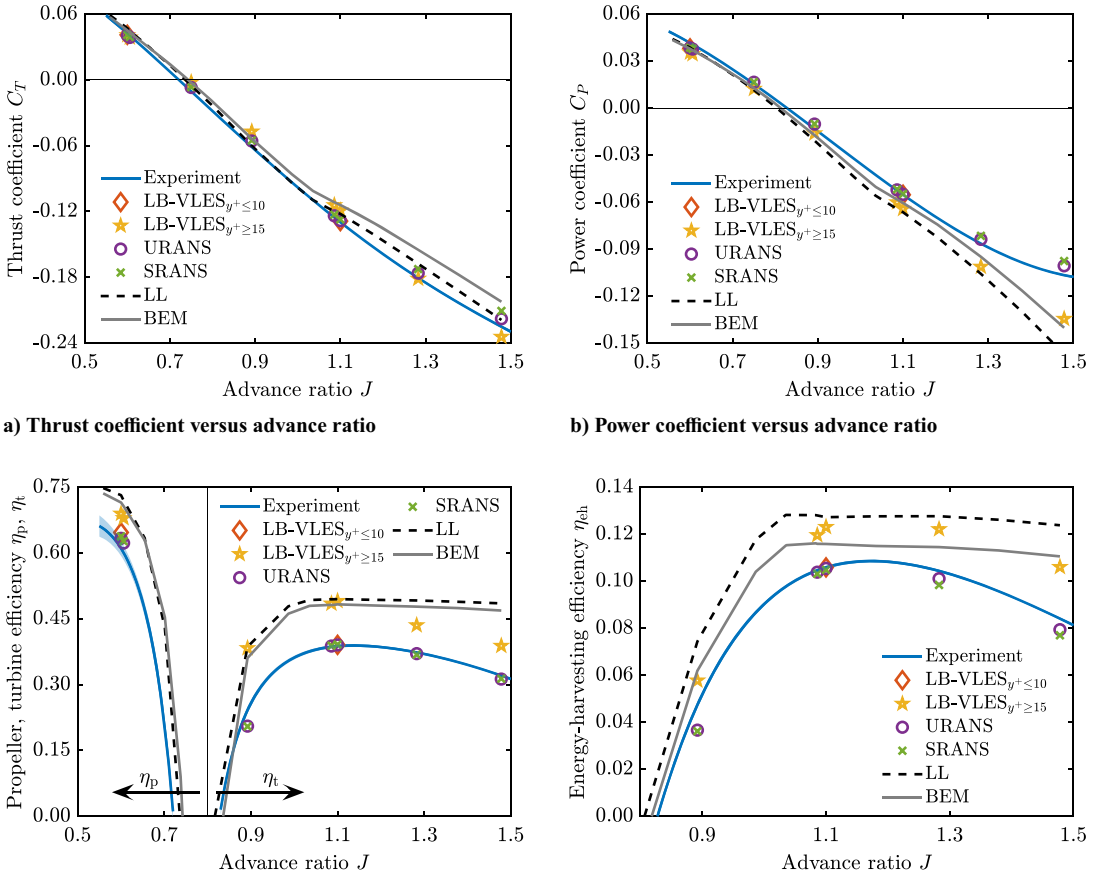

a) Thrust coefficient versus advance ratio

b) Power coefficient versus advance ratio

c) Propeller and turbine efficiency versus advance ratio

d) Energy-harvesting efficiency versus advance ratio

Fig. 7 Comparison of integrated performance estimated using different numerical methods with the experimental data.

Table 6 Integrated performance of the propeller at the positive thrust condition ($J = 0.60$) calculated using different methods

Method	C_T	$\Delta C_T\%$	C_P	$\Delta C_P\%$	η_p	$\Delta\eta_p\%$
Experiment	0.04234 ± 0.00103	$\pm 2.44\%$	0.04160 ± 0.00056	$\pm 1.35\%$	0.6107 ± 0.0171	$\pm 2.79\%$
LB-VLES$_{y^+\leq 10}$	0.04109	-2.96%	0.03810	-8.40%	0.6469	$+5.93\%$
LB-VLES$_{y^+\geq 15}$	0.04085	-3.51%	0.03554	-14.58%	0.6898	$+12.95\%$
URANS	0.04055	-4.22%	0.03841	-7.66%	0.6335	$+3.73\%$
SRANS	0.04097	-3.23%	0.03853	-7.39%	0.6381	$+4.48\%$
LL	0.04713	$+11.31\%$	0.03864	-7.12%	0.7318	$+19.84\%$
BEM	0.04512	$+6.56\%$	0.03785	-9.01%	0.7152	$+17.11\%$

Table 7 Integrated performance of the propeller at the negative thrust condition ($J = 1.10$) calculated using different methods

Method	C_T	$\Delta C_T\%$	C_P	$\Delta C_P\%$	η_t	$\Delta\eta_t\%$
Experiment	-0.12978 ± 0.00069	$\pm 0.53\%$	-0.05534 ± 0.00035	$\pm 0.63\%$	0.3877 ± 0.0032	$\pm 0.83\%$
LB-VLES$_{y^+\leq 10}$	-0.12878	-0.77%	-0.05535	$+0.01\%$	0.3907	$+0.79\%$
LB-VLES$_{y^+\geq 15}$	-0.11918	-8.17%	-0.06434	$+16.26\%$	0.4908	$+26.61\%$
URANS	-0.12835	-1.11%	-0.05514	-0.37%	0.3905	$+0.74\%$
SRANS	-0.12724	-1.96%	-0.05480	-0.98%	0.3915	$+1.00\%$
LL	-0.12217	-5.87%	-0.06651	$+20.18\%$	0.4949	$+27.67\%$
BEM	-0.11398	-12.18%	-0.06056	$+9.42\%$	0.4830	$+24.60\%$

Downloaded by Technische Universiteit Delft on October 7, 2024 | http://arc.aiaa.org | DOI: 10.2514/1.J064093

performance calculated using different numerical tools as compared to the experimental data for a positive ($J = 0.60$) and a negative thrust condition ($J = 1.10$), respectively. The uncertainties in the experimental data calculated for a 95% confidence interval are depicted by the shaded-blue region in the figure and as "±" values in the tables. However, the shaded blue region is only visible for η_p in Fig. 7 due to the small values of uncertainty for other parameters.

Figures 7a and 7b show the comparison of C_T versus J and C_P versus J, respectively. The uncertainty (95% confidence interval) in the experimental C_T and C_P values at $J = 0.60$ is ±2% and ±3%, respectively. The LB-VLES$_{y^+\leq 10}$, available only for two operating points, display a good agreement with the experiment for C_T at both conditions, with a 3% error at the positive thrust condition ($J = 0.60$) and less than 1% error at the negative thrust condition ($J = 1.10$). In contrast, C_P shows an 8% error at the positive thrust condition ($J = 0.60$) and almost no error at the negative thrust condition ($J = 1.10$) compared to the experiment (see Tables 6 and 7).

The LB-VLES$_{y^+\geq 15}$ follow the trend of variation of C_T with J for the whole range of advance ratios, as can be seen in Fig. 7a. However, the same cannot be said for C_P (see Fig. 7b). These simulations significantly overpredict C_P beyond the maximum power output point ($J > 1.10$), reaching up to a 26% deviation at $J = 1.48$ compared to the experiment. Closer examination (Table 6) reveals underpredictions of both C_T and C_P by approximately 4% and 15%, respectively, at the positive thrust condition ($J = 0.60$). In contrast, the negative thrust condition ($J = 1.10$) exhibits a considerable increase in errors (Table 7), reaching 8% and 16% for C_T and C_P, respectively. These significant inaccuracies, particularly for $J \geq 1.10$, are likely caused by the delayed transition from modeled to resolved turbulence, leading to errors in predicting complex flow phenomena such as separation and reattachment. This argument is further supported by the superior agreement of LB-VLES$_{y^+\leq 10}$ with experimental data at $J = 1.10$ compared to LB-VLES$_{y^+\geq 15}$. Section IV.B will discuss this in more detail.

The SRANS and URANS simulations show near-identical solutions in the positive thrust regime ($J = 0.60$), showing errors of approximately 3–4% for C_T and 7–8% for C_P (see Table 6). The significant underprediction of C_P by the RANS, as well as LB-VLES simulations at $J = 0.60$, is expected to be a consequence of the lower drag prediction in the simulations than experiment. In contrast, at the negative thrust condition near the maximum power output point ($J = 1.10$), the errors in both C_T (1–2%) and C_P (less than 1%) drop significantly compared to the positive thrust regime (see Table 7).

The differences between SRANS and URANS simulations become more pronounced as the advance ratio increases in the negative thrust regime (Figs. 7a and 7b). The rising discrepancies between the two highlight the growing significance of unsteadiness with an increasing advance ratio due to the increase in flow separation in the negative thrust regime. Moreover, the errors in C_T and C_P values for URANS simulations, relative to the experiment, increase with the increase in the advance ratio. For instance, at $J = 1.48$, the errors in C_T and C_P values increase to 3% and 6%, respectively. The increasing error can be attributed to the inaccuracies introduced by turbulence modeling in URANS simulations.

While negative thrust conditions were expected to be more challenging to simulate, comparisons of Tables 6 and 7 show that mid- and high-fidelity simulations (except for LB-VLES$_{y^+\geq 15}$) exhibit higher errors for the positive thrust condition ($J = 0.60$) than the negative thrust condition ($J = 1.10$). This unexpected trend can be attributed to the operation of the propeller at a relatively low Reynolds number based on chord and effective velocity (2×10^5–3×10^5) for these operating conditions. As a result, laminar separation bubbles are likely present in the experiments, whereas the simulations assume a fully turbulent flow. The presence of laminar separation bubbles in the experiments leads to a higher drag compared to the mid- and high-fidelity simulations, resulting in the observed differences for the positive thrust condition. This effect was verified by estimating the performance of blade sections using XFOIL with and without forced transition. Additionally, experimental measurements show a negative total pressure coefficient C_{p_t} at the blade tip (discussed later in Sec. IV.C.1), which is not replicated in the mid- and high-fidelity simulations, further amplifying the difference in the experimental and simulated integrated performance for the positive thrust condition.

In contrast, the negative thrust condition ($J = 1.10$) experiences flow separation along most of the blade span (shown later in Sec. IV.B.2). Fully separated flows are comparatively easier to simulate than the prediction of laminar separation bubbles. Consequently, a closer match between experiments and mid- and high-fidelity simulations (except for LB-VLES$_{y^+\geq 15}$) is observed for the negative thrust condition ($J = 1.10$) compared to the positive thrust condition ($J = 0.60$).

The low-fidelity tools BEM and LL showcase a reasonable agreement with experimental gradients for both C_T and C_P with respect to J up to $J \leq 1.10$ (close to the maximum power output point) (see Figs. 7a and 7b). However, as the advance ratio increases further, both tools struggle to capture even the gradients accurately for both C_T and C_P with respect to J. In the positive thrust regime ($J = 0.60$), the LL model overestimates C_T by 11% and underestimates C_P by 7% (see Table 6). At the negative thrust condition ($J = 1.10$), the error in C_T reduces to 6%, but with a significant jump in C_P error to 20%, as listed in Table 7. The BEM model exhibits a rise in C_T error from 7% to 12% between $J = 0.60$ and $J = 1.10$, while the error in C_P stays almost unaffected (9%) across both advance ratios.

The underprediction of $|C_T|$ and overprediction of $|C_P|$ by BEM and LL for $J \geq 1.10$ is expected to be the consequence of neglecting 3D flow effects in BEM and LL theories and their impact on the boundary layer of blade sections, resulting in a delayed stall prediction in RFOIL [20,21].

Figure 7c shows the variation of propeller efficiency for positive thrust conditions and turbine efficiency for negative thrust conditions. The LB-VLESs$_{y^+\leq 10}$ show errors of 6% and 1% compared to experimental data for positive and negative thrust conditions, respectively. The higher error at $J = 0.60$ (positive thrust) can be traced back to the 8% underprediction of C_P in this simulation. However, the LB-VLESs$_{y^+\geq 15}$ consistently overpredict both propeller and turbine efficiency across the entire advance ratio range, with overpredictions of 13% at $J = 0.60$ and 27% at $J = 1.10$. This significant overestimation of turbine efficiency directly reflects the overprediction of C_P values in this simulation setup. While the absolute values are inaccurate, it is worth noting that these simulations still capture the overall gradients of turbine efficiency with J, as shown in Fig. 7c.

As SRANS and URANS simulations are in reasonable agreement with the experimental data for C_T and C_P in Figs. 7a and 7b, it results in a reasonable agreement for propeller and turbine efficiencies over the whole range of advance ratio (see Fig. 7c). The RANS simulations show an error of 4–5% for propeller efficiency at $J = 0.60$ and less than 1% error for turbine efficiency at $J = 1.10$ (see Tables 6 and 7). BEM and LL methods manage to capture the gradient of propeller efficiency with respect to J but with an offset in values compared to experimental data. The significant offset, with BEM and LL predicting 17–20% higher propeller efficiency than the experiment at $J = 0.60$, cannot be only due to the errors in the profile performance (L/D ratio) predicted by RFOIL but is also a consequence of the incorrect induction predictions by BEM and LL theories leading to incorrect inflow angles. In contrast, BEM and LL fail to capture the gradients of turbine efficiency with respect to J altogether, with their predictions flattening out as the advance ratio increases for $J \geq 1.10$.

Figure 7d shows the energy-harvesting efficiency of the propeller obtained using the different methods. At the negative thrust condition ($J = 1.10$), the LB-VLES$_{y^+\leq 10}$ closely aligns with the experimental value, as also expected from C_P values in Table 7. This remarkable agreement highlights the effectiveness of this simulation setup in capturing complex flow phenomena under challenging operating conditions. In contrast, the LB-VLESs$_{y^+\geq 15}$ significantly overestimate energy-harvesting efficiency (by 16% at $J = 1.10$) compared to the experiment. Such a stark difference between LB-VLES$_{y^+\leq 10}$ and LB-VLESs$_{y^+\geq 15}$ at $J = 1.10$ is a consequence of significant flow separation around the blade at this operating condition, making it necessary to accurately capture separation and resolve turbulence at this operating condition. While the absolute values may be overpredicted, it is noteworthy that the LB-VLESs$_{y^+\geq 15}$ still capture the overall gradients of energy-harvesting efficiency with J.

The SRANS and URANS simulations, on the other hand, deliver consistently close predictions to the experiments across the entire advance ratio range, with errors of 6–8% at $J = 1.48$ (Fig. 7d). Similar to the gradients observed for turbine efficiency with respect to J in Fig. 7c, both BEM and LL methods generate an almost flat line for energy-harvesting efficiency in Fig. 7d for $J \geq 1.10$. This indicates that BEM and LL can only be used up to a certain advance ratio in negative thrust conditions (up to the maximum power output point in this case).

B. Flow Around the Propeller Blades

This section describes the complexity of the flow phenomena around the propeller blades that is the cause of inaccurate performance predictions by BEM, LL, and LB-VLESs$_{y^+\geq 15}$. Figure 8 shows the contours of the skin-friction coefficient C_f on the blade surface along with shearlines for $J = 0.60$ (positive thrust) for the mid- and high-fidelity simulations. The figure also displays flow streamlines at three radial stations: $r/R = 0.3$, 0.6, and 0.9. Complementing these visualizations, Fig. 9 presents chordwise pressure distributions (C_{p_s}) at the aforementioned radial stations for $J = 0.60$. Similarly, Figs. 10 and 11 show the skin-friction coefficient contours (C_f) and chordwise pressure distributions (C_{p_s}) for $J = 1.10$ (negative thrust).

C_{p_s} is defined based on the local dynamic pressure calculated using the effective velocity ($V_{\text{eff}} = \sqrt{V_\infty^2 + (\Omega r)^2}$). The chordwise pressure distributions for BEM and LL have been obtained using RFOIL. To ensure clarity and conciseness, URANS data have been omitted from the chordwise pressure distribution comparisons, as SRANS and URANS show almost identical solutions in Figs. 8 and 10, and thus the pressure distributions were also almost identical.

To quantify the discrepancies in chordwise pressure distributions across different numerical methods, the normal-force coefficient was calculated by integrating the chordwise pressure distributions with normalized chordwise coordinates (ζ/c). The resulting values of the normal-force coefficient ($C_{\text{n}} = \int_0^1 C_{p_s}\, \mathrm{d}\zeta/c$) for $J = 0.60$ and $J = 1.10$ are listed in Tables 8 and 9, respectively. Considering the LB-VLESs$_{y^+\leq 10}$ as the reference, the relative change in the normal-force coefficient was calculated as follows:

$$\Delta C_{\text{n}}\% = \frac{C_{\text{n}_{\text{method}}} - C_{\text{n}_{\text{LB-VLES}_{y^+\leq 10}}}}{C_{\text{n}_{\text{LB-VLES}_{y^+\leq 10}}}} \times 100 \tag{2}$$

1. *Positive Thrust Condition ($J = 0.60$)*

Figure 8 shows the visualization of flow around the propeller blades at $J = 0.60$ as predicted by SRANS, URANS, LB-VLES$_{y^+\geq 15}$ and LB-VLESs$_{y^+\leq 10}$. Notably, SRANS and URANS simulations yield nearly identical solutions, both indicating the presence of a leading-edge separation bubble on the back side of the blade, primarily in the outboard region. This is evident from the shearlines (see Figs. 8a and 8b). The reattachment location along the blade span for different simulations is indicated in the figure using dashed cyan-colored lines.

In contrast, the LB-VLES$_{y^+\geq 15}$ shows a separation bubble extending up to $r/R \approx 0.4$ on both sides of the blade, as evident from the shearlines in Fig. 8c. Another interesting phenomenon that can be noticed in Fig. 8c is the radial outboard pumping of the flow when the flow is separated or about to separate. The centrifugal force pushes the flow in stagnant regions toward the tip, which results in a Coriolis force and acts as a favorable pressure gradient, delaying the stall and resulting in higher lift coefficients compared to a nonrotating blade. This phenomenon is known as the Himmelskamp effect [44] and is shown along the blade span in the figure using dashed yellow-colored lines.

Figure 8d shows the flow around the propeller blades predicted by LB-VLES$_{y^+\leq 10}$ for $J = 0.60$. The skin friction contours seem more discontinuous compared to other simulations. This can be attributed to the increased surface resolution in LB-VLES$_{y^+\leq 10}$, which allows the capture of small-scale flow fluctuations that remain unresolved in the other simulations. The LB-VLES$_{y^+\leq 10}$ also exhibits a separation bubble in the inboard sections, similar to the LB-VLES$_{y^+\geq 15}$. In addition, the LB-VLES$_{y^+\leq 10}$ shows small separation bubbles in outboard sections very close to the leading edge on the back side of the blade. These outboard characteristics resemble those observed in RANS simulations, albeit with somewhat reduced intensity. These separation bubbles are the result of the operation of the propeller at low Reynolds numbers. The presence of the separation bubbles makes it challenging to have a good agreement between different numerical methods due to the sensitivity of the separation bubble length to the resolution of the boundary layer (y^+) besides other

Downloaded by Technische Universiteit Delft on October 7, 2024 | http://arc.aiaa.org | DOI: 10.2514/1.J064093

Downloaded by Technische Universiteit Delft on October 7, 2024 | http://arc.aiaa.org | DOI: 10.2514/1.J064093

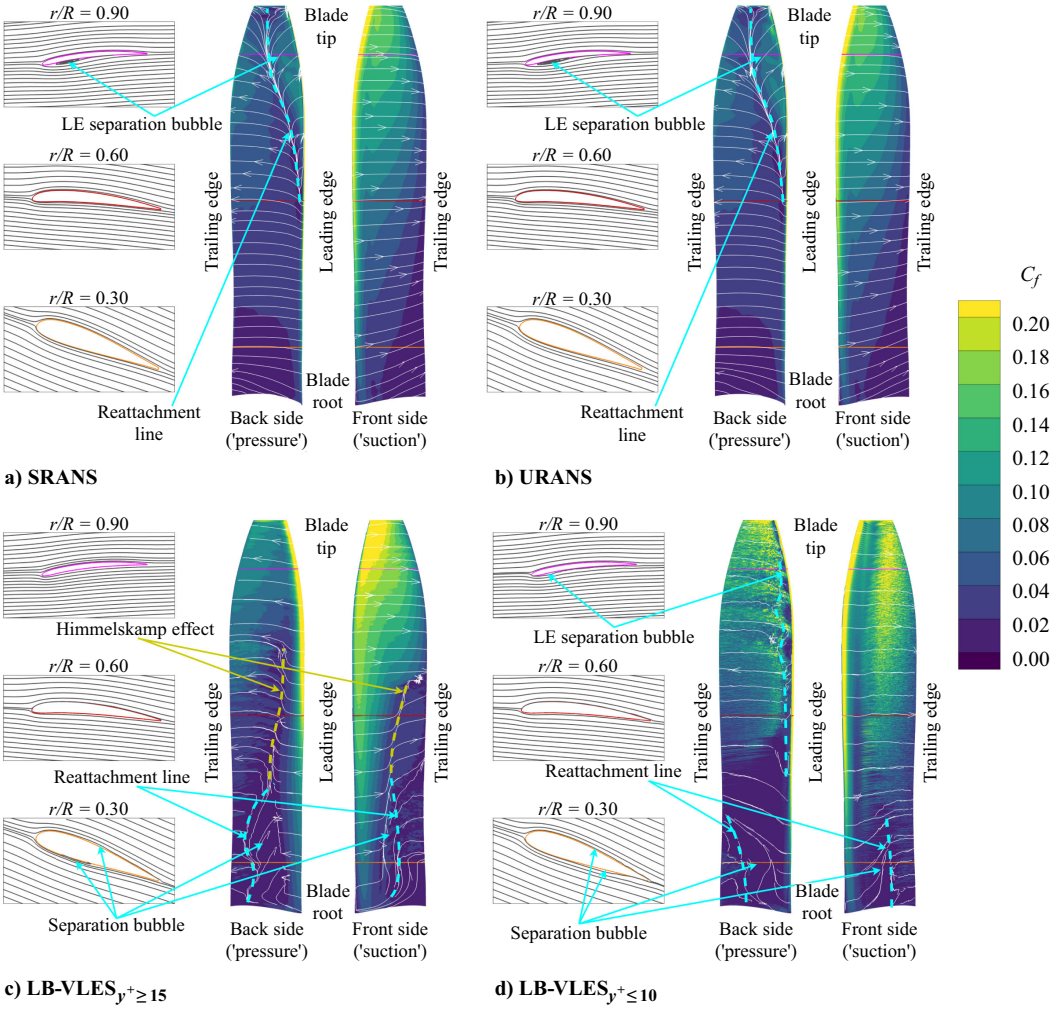

Fig. 8 Visualization of flow around propeller blades at the positive thrust condition ($J = 0.60$) using skin friction coefficient and shear lines.

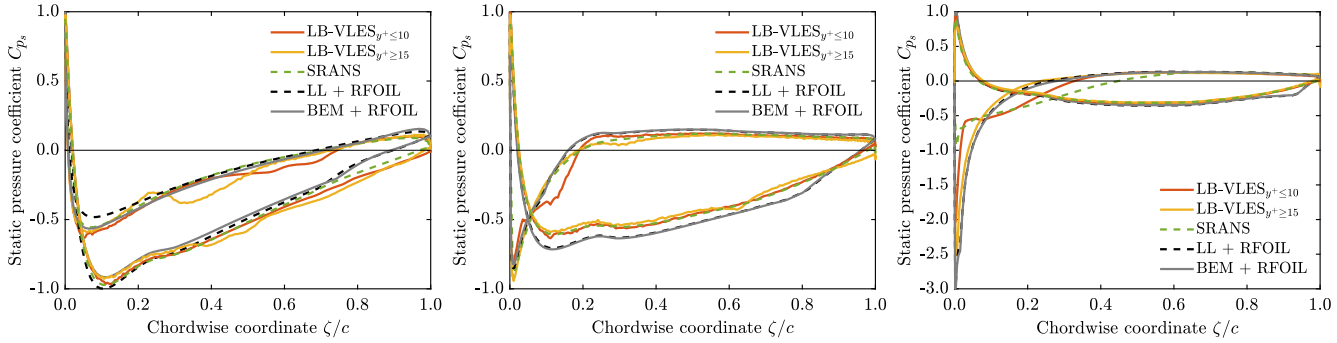

a) $r/R = 0.30$ **b) $r/R = 0.60$** **c) $r/R = 0.90$**

Fig. 9 Chordwise pressure coefficient distributions (C_{p_s}) at the positive thrust condition ($J = 0.60$).

parameters, such as incoming turbulence, surface roughness, and subgrid-scale modeling [45–48].

The chordwise pressure distributions (C_{p_s}) at different radial stations offer further insights into the discrepancies between the solutions obtained from the different methods. At $r/R = 0.30$, separation bubbles in LB-VLES simulations are evident in the chordwise pressure distribution (see Fig. 9a). The size and location of the predicted separation bubble are observed to be sensitive to the boundary-layer resolution (LB-VLES$_{y^+\leq 10}$ vs LB-VLES$_{y^+\geq 15}$ results), as anticipated. In contrast, the SRANS simulation does not predict any separation bubble, resulting in a chordwise pressure distribution similar to those obtained using BEM and LL theories combined with RFOIL, with the exception of the solution near the trailing edge. Notably, the chordwise pressure distribution from the SRANS simulation at the trailing edge matches that of the LB-VLES simulations, suggesting a possible similarity in the vortices shed at the trailing edge.

The differences in chordwise pressure distributions are quantified in Table 8. The differences in separation bubble size and location in LB-VLES simulations result in a 3% difference in the normal-force coefficient at $r/R = 0.30$ between the two LB-VLES approaches. Compared with the LB-VLES$_{y^+\leq 10}$ as the reference, the SRANS simulation predicts an 8% higher normal-force coefficient at $r/R = 0.30$ due to the absence of a separation bubble. The LL and BEM theories, coupled with RFOIL, predict 8% higher and 12% lower normal-force coefficients, respectively, compared to the

Downloaded by Technische Universiteit Delft on October 7, 2024 | http://arc.aiaa.org | DOI: 10.2514/1.J064093

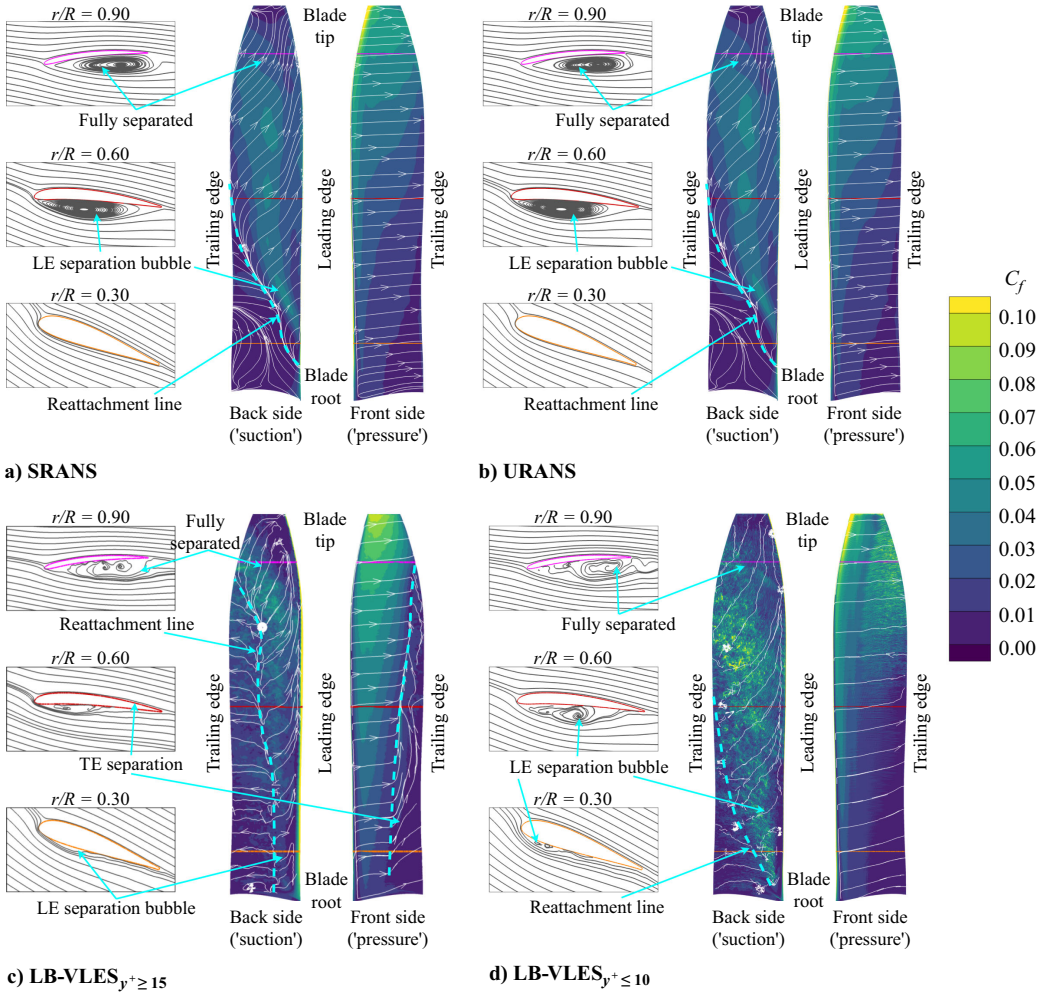

Fig. 10 Visualization of flow around propeller blades at the negative thrust condition ($J = 1.10$) using skin friction coefficient and shear lines.

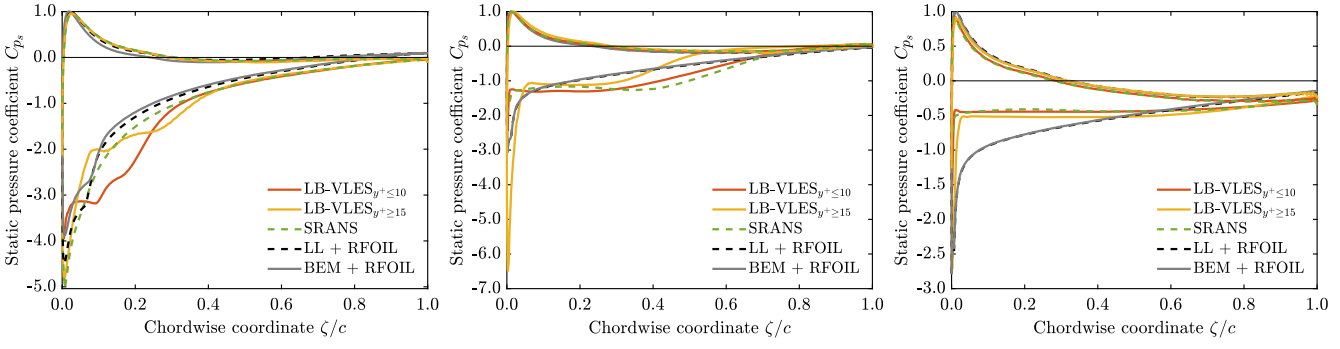

Fig. 11 Chordwise pressure coefficient distributions (C_{p_s}) at the negative thrust condition ($J = 1.10$).

Table 8 Normal-force coefficient C_n at different radial stations at the positive thrust condition ($J = 0.60$)

	$r/R = 0.30$		$r/R = 0.60$		$r/R = 0.90$	
Method	C_n	ΔC_n%	C_n	ΔC_n%	C_n	ΔC_n%
LB-VLES$_{y^+\leq 10}$	−0.2861	——	−0.3794	——	−0.1213	——
LB-VLES$_{y^+\geq 15}$	−0.2934	+2.53%	−0.3614	−4.73%	−0.1285	+5.94%
SRANS	−0.3101	+8.39%	−0.3870	+2.01%	−0.1002	−17.34%
LL + RFOIL	−0.3088	+7.93%	−0.4750	+25.21%	−0.1454	+19.92%
BEM + RFOIL	−0.2509	−12.31%	−0.4820	+27.04%	−0.1279	+5.49%

Table 9 Normal-force coefficient C_n at different radial stations at the negative thrust condition ($J = 1.10$)

	$r/R = 0.30$		$r/R = 0.60$		$r/R = 0.90$	
Method	C_n	$\Delta C_n\%$	C_n	$\Delta C_n\%$	C_n	$\Delta C_n\%$
LB-VLES$_{y^+\leq 10}$	1.0981	— —	0.7261	— —	0.3430	— —
LB-VLES$_{y^+\geq 15}$	0.9990	−9.02%	0.6033	−16.91%	0.4599	+34.08%
SRANS	1.0171	−7.38%	0.7727	+6.41%	0.3282	−4.32%
LL + RFOIL	0.9017	−17.89%	0.6053	−16.63%	0.5462	+59.23%
BEM + RFOIL	0.7890	−28.15%	0.5878	−19.04%	0.5349	+55.92%

LB-VLES$_{y^+\leq 10}$. The significantly lower normal-force coefficient in BEM theory, compared to LL theory, is suspected to be a consequence of the higher hub loss in BEM theory calculated through the Prandtl tip and hub loss correction. This higher hub loss results in a lower angle of attack and, consequently, a lower normal-force coefficient than LL theory.

At $r/R = 0.60$, the LB-VLES$_{y^+\leq 10}$ exhibits a small leading-edge separation bubble, consistent with earlier observations in Fig. 8d. This feature is absent in other numerical methods. The LB-VLES$_{y^+\geq 15}$, influenced by the Himmelskamp effect, shows a thicker boundary layer at the trailing edge compared to LB-VLES$_{y^+\leq 10}$ (Fig. 9b), resulting in a 5% lower normal-force coefficient (Table 9). The SRANS simulation, lacking the leading-edge bubble, differs by 2% compared to LB-VLES$_{y^+\leq 10}$. In contrast, both LL and BEM theories, with their overestimation of suction force, show an overestimation of the normal-force coefficient by 25% and 27%, respectively, compared to the LB-VLES$_{y^+\leq 10}$. This increased suction force could result from either an inaccurate prediction of the angle of attack by BEM and LL theories, or an inaccurate prediction of blade section performance by RFOIL at a given angle of attack, or a combination of both of these factors.

Significant differences can be seen in the chordwise pressure distribution at $r/R = 0.90$ near the leading edge (see Fig. 9c). Both SRANS and LB-VLESs$_{y^+\leq 10}$ predict a leading-edge separation bubble, consistent with the visualization in Fig. 8. The differences in the size and location of these bubbles result in a notable difference in chordwise pressure distributions up to $\zeta/c = 0.6$. These differences in chordwise pressure distributions translate to a 17% lower normal-force coefficient for the SRANS simulation compared to the LB-VLES$_{y^+\leq 10}$. Interestingly, the absence of a leading-edge separation bubble in the LB-VLES$_{y^+\geq 15}$ results in almost identical chordwise pressure distributions as predicted using BEM and LL theories combined with RFOIL.

These observations underscore the significance of accurately predicting separation bubbles in simulations and highlight the critical role of boundary-layer resolution in capturing complex flow phenomena. Despite the apparent inability of BEM and LL theories combined with RFOIL to capture the separation bubbles accurately, these methods offer a qualitatively reasonable estimate of chordwise pressure distributions for all considered radial stations at $J = 0.60$. The quantitative differences between the normal-force coefficient obtained from BEM and LL theories combined with RFOIL and LB-VLESs$_{y^+\leq 10}$ may have been aggravated due to the selected case for which the blade sections were operating at a low Reynolds number.

2. *Negative Thrust Condition ($J = 1.10$)*

Figure 10 shows the visualization of flow around the propeller blades at $J = 1.10$ as predicted by SRANS, URANS, LB-VLES$_{y^+\geq 15}$ and LB-VLESs$_{y^+\leq 10}$. Once again, SRANS and URANS simulations exhibit near-identical solutions despite flow separation in the outboard section of the blade, as evident in Figs. 10a and 10b. This separation, attributed to the operation at negative angles of attack, manifests as a leading-edge separation bubble in the inboard sections on the back side of the blade. This bubble progressively expands toward the tip, leading to complete flow separation beyond $r/R = 0.60$.

On the other hand, the LB-VLES$_{y^+\geq 15}$ predicts that the separation bubble reaches the trailing edge at $r/R = 0.85$ (see Fig. 10c). Additionally, the LB-VLES$_{y^+\geq 15}$ also predicts trailing-edge separation on the front side of the blade, which is not observed in other methods.

Interestingly, the LB-VLES$_{y^+\leq 10}$ in Fig. 10d predicts similar results as seen in the RANS simulations, i.e., a leading-edge separation bubble in the inboard sections on the back side of the blade extending to the trailing edge at around $r/R = 0.60$. Unlike the LB-VLES$_{y^+\geq 15}$, no trailing-edge separation is predicted on the front side of the blade in the LB-VLES$_{y^+\leq 10}$. As the flow stays attached up to a higher radial coordinate in the LB-VLES$_{y^+\geq 15}$ (Fig. 10c), it leads to higher $|C_P|$ compared to the RANS and LB-VLESs$_{y^+\leq 10}$ as shown before in Fig. 7b.

Expanding this analysis further, the chordwise pressure distributions (C_{p_s}) are compared in Fig. 11 and the resulting normal-force coefficients are listed in Table 9. At $r/R = 0.30$, BEM and LL theories combined with RFOIL show a leading-edge separation bubble similar to that observed in mid- and high-fidelity simulations (Fig. 11a). However, the size of this bubble is notably smaller in BEM and LL theories combined with RFOIL, leading to underestimations of the normal-force coefficient by 28% and 18% compared to the LB-VLES$_{y^+\leq 10}$ (Table 9). Similarly, the difference in size and location of the separation bubbles in the LB-VLES$_{y^+\geq 15}$ and SRANS simulations as compared to the LB-VLES$_{y^+\leq 10}$ results in 9% and 7% lower normal-force coefficient, respectively.

The difference in the size and location of the separation bubbles at $r/R = 0.60$ is evident in the chordwise pressure distributions of the SRANS and LB-VLES simulations in Fig. 11b. While the SRANS simulation exhibits a separation bubble size similar to the LB-VLES$_{y^+\leq 10}$, the significant difference in the suction peak magnitude results in a 6% normal-force underestimation compared to the LB-VLES$_{y^+\leq 10}$. The LB-VLES$_{y^+\geq 15}$, on the other hand, showcases a smaller separation bubble and higher suction peak, leading to a 17% underestimation of the normal-force coefficient compared to the LB-VLES$_{y^+\leq 10}$. In contrast, the chordwise pressure distributions from BEM and LL theories combined with RFOIL do not predict any separation bubble, resulting in a 19 and 17% lower normal-force coefficient, respectively, compared to the LB-VLES$_{y^+\leq 10}$.

At $r/R = 0.90$ in Fig. 11c, the SRANS and both LB-VLES simulations predict qualitatively similar chordwise pressure distributions, indicating diminishing discrepancies as the flow fully separates. Despite the qualitative similarity, the LB-VLES$_{y^+\geq 15}$ predicts a 34% higher normal-force coefficient compared to the LB-VLES$_{y^+\leq 10}$ due to its higher suction and pressure values. In contrast to higher-fidelity simulations, the chordwise pressure distributions from BEM and LL theories combined with RFOIL predict attached flow without a separation bubble, resulting in a 56% and 59% higher normal-force coefficient, respectively, compared to the LB-VLES$_{y^+\leq 10}$. This observation substantiates the delayed stall prediction in RFOIL is a contributing factor to the underprediction of $|C_T|$ and the overprediction of $|C_P|$ by BEM and LL in negative thrust conditions, as shown in Figs. 7a and 7b.

Considering the LB-VLES$_{y^+\leq 10}$ as the reference, it is evident that RANS modeling with a resolved boundary layer can provide more accurate predictions of mean flow characteristics compared to the LB-VLES$_{y^+\geq 15}$. This is an expected conclusion given the extent of separation along the propeller blade, making it necessary to either

Downloaded by Technische Universiteit Delft on October 7, 2024 | http://arc.aiaa.org | DOI: 10.2514/1.J064093

Downloaded by Technische Universiteit Delft on October 7, 2024 | http://arc.aiaa.org | DOI: 10.2514/1.J064093

resolve the boundary layer (as done in RANS simulations) or to use the enhanced modeled to resolved turbulence transition capabilities of the LB-VLES (PowerFLOW) solver by ensuring $y^+ \leq 10$ [35]. The BEM and LL theories combined with RFOIL provide a qualitatively reasonable chordwise pressure distribution for the blade sections where the flow remains attached ($r/R = 0.30$). However, these models prove to be inadequate for the blade sections with fully separated flow due to their inherent assumptions of 2D flow, leading to significant errors, as seen for $r/R = 0.90$ for this operating condition.

C. Total Pressure Coefficient and Blade Loading

Besides integrated performance, the radial blade loading distributions are essential inputs for studies in aeroacoustics and optimization. Therefore, evaluating the predictive accuracy of numerical tools in capturing blade loading distributions is essential. However, directly measuring blade loading through experiments remains a challenge. Instead, the radial distributions of the total pressure coefficient C_{p_t} measured using a five-hole pressure probe at a fixed azimuthal position at $x/R = 0.15$ downstream of the propeller offer an indirect measure of blade loading. The total pressure coefficient profiles obtained using different numerical methods have been compared with the experimental data for the same advance ratios considered in the preceding section: $J = 0.60$ and 1.10 (positive and negative thrust, respectively). As the flow is still expected to be partially attached at $J = 1.10$ (Fig. 10), blade loading has also been evaluated for $J = 1.48$ to understand how the differences between numerical methods are affected when the flow is fully separated along the whole blade span. Note that experimental total pressure coefficient profiles for $J = 1.48$ are unavailable, and therefore, for this condition, only a comparison between the different numerical solutions is available.

The total pressure coefficient profiles for SRANS, URANS, LB-VLES$_{y^+\geq 15}$ and LB-VLESs$_{y^+\leq 10}$ are directly available from the simulation data. However, BEM and LL require alternative methods. Given the close proximity of the measurement location to the propeller plane of rotation ($x/R = 0.15$), the change in total pressure across the propeller can be estimated from the thrust distribution as outlined in Eq. (4). This approach neglects the contribution of the swirl, viscous losses, and slipstream contraction at the measurement location. The assumption of no contraction is at least partially mitigated by the flow displacement due to the nacelle thickness.

$$\delta P(r) = \frac{\delta T(r)}{2\pi r \delta r} \tag{3}$$

$$C_{p_t}(r) = \frac{\delta P(r)}{q_\infty} \tag{4}$$

1. *Positive Thrust Condition ($J = 0.60$)*

Figure 12a shows the comparison of the radial distribution of the total pressure coefficient at $0.15R$ downstream of the propeller center for $J = 0.60$. The solid blue line represents the experimental data, with a shaded blue area denoting the estimated experimental uncertainty (estimated to be around 3% at the peak value). The BEM prediction shows agreement with the experimental total pressure distribution, with a 6% overprediction of the peak. Additionally, BEM predicts a negative total pressure coefficient for $0.95 \leq r/R \leq 1$, whereas the experiment shows a negative total pressure coefficient between $0.92 \leq r/R \leq 1$. Similarly, the LL method overestimates the peak value by 5% as compared to the experiment and predicts a negative total pressure coefficient for $0.97 < r/R \leq 1$. The overprediction of the total pressure coefficient by the BEM and LL theories is in agreement with the observed overprediction of C_T with respect to the experiment, as listed in Table 6.

In contrast to the BEM and LL theories, all the higher-fidelity simulations underpredict the peak total pressure coefficient value compared to the experimental data. Both SRANS and URANS simulations show an 11% underprediction of the peak, while LB-VLES$_{y^+\leq 10}$ and LB-VLESs$_{y^+\geq 15}$ underestimate the peak by 12% and 16%, respectively. Additionally, the SRANS and URANS simulations fail to capture the negative total pressure coefficient observed in the experiment at $0.92 \leq r/R \leq 1$. In both the LB-VLES simulations, the total pressure coefficient is negative only between $0.98 \leq r/R \leq 1$. The underprediction of the total pressure coefficient is in agreement with the previously seen underprediction of C_T and C_P by the mid- and high-fidelity simulations in Table 6.

The total pressure distribution seems to be better predicted by BEM and LL theories, even though these models exhibit higher discrepancies in integrated performance compared to higher-fidelity simulations (Table 6). This seemingly contradictory observation can be attributed to multiple effects.

The mid- and high-fidelity simulations do not predict the negative C_{p_t} at the blade tip observed in the experiments. This negative C_{p_t} indicates negative thrust being produced by the blade tip in the experiments. Consequently, this would lead to a higher underestimation of the blade loading peak/total pressure peak by simulations compared to experiments than the underprediction of the integrated thrust listed in Table 6. Besides, the lower predicted power in the mid- and high-fidelity simulations translates to underpredicted momentum added to the flow in the swirl direction. This underprediction of swirl momentum contributes to increasing the discrepancy in the total pressure peak observed in higher-fidelity simulations compared to experiments.

In contrast, two effects are neglected in the calculation of the total pressure coefficient for BEM and LL theories, which, if accounted for, would lead to a greater overprediction of the total pressure coefficient than is currently observed. The first is the neglect of the swirl momentum, which is estimated to account for an additional 1–2% of the total pressure coefficient (away from root and tip) based on SRANS results. Secondly, BEM and LL theories do not account for slipstream contraction, which would further increase the overprediction of the peak value of C_{p_t}. These effects are partially countered by neglecting the viscous losses and slipstream displacement due to the presence of the nacelle. This neglect of all these effects combined results in the observed 5–6% overprediction of the

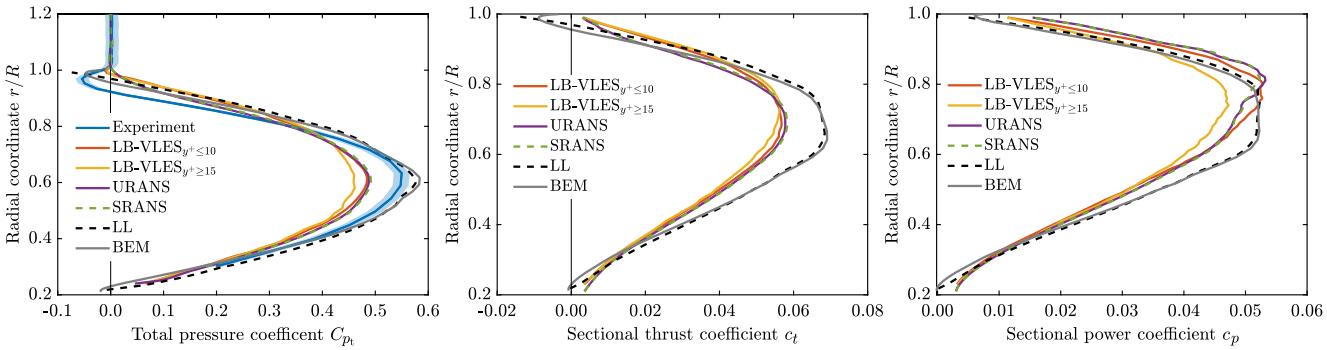

a) Total pressure coefficient **b) Thrust distribution** **c) Power distribution**

Fig. 12 Total pressure coefficient C_{p_t} at $0.15R$ downstream of propeller center and blade loading at the positive thrust condition ($J = 0.60$).

Downloaded by Technische Universiteit Delft on October 7, 2024 | http://arc.aiaa.org | DOI: 10.2514/1.J064093

peak value of C_{p_t} by BEM and LL theories as compared to experiments.

Figures 12b and 12c present the thrust and power distribution along the propeller blade for $J = 0.60$, respectively. Since the total pressure coefficient and thrust distributions are interconnected through Eq. (4), discrepancies in thrust distribution mirror those observed in the total pressure coefficient profile. Interestingly, the viscous losses in the tip vortices lead to a positive thrust and power in the outboard region despite the negative total pressure coefficients in this region.

In terms of power distribution along the blade span, the RANS and LB-VLESs$_{y^+\leq 10}$ show similar results, except that the RANS simulations predict the peak location to be slightly outboard (at $0.80R$) compared to the LB-VLES$_{y^+\leq 10}$ (at $0.75R$). The LB-VLES$_{y^+\geq 15}$ predicts a power distribution profile similar to the LB-VLES$_{y^+\leq 10}$, but the peak loading of the former is underpredicted by 10% compared to the latter. BEM and LL predict a higher inboard torque loading and a lower outboard torque loading than the higher-fidelity simulations. Also, the power peak is inboard (at $0.65R$) compared to higher-fidelity simulations (around $0.75R - 0.80R$).

2. *Negative Thrust Conditions ($J = 1.10, 1.48$)*

The comparison of the total pressure coefficient and blade loading for the negative thrust condition with $J = 1.10$ can be seen in Fig. 13. As mentioned before, this advance ratio is close to the point of maximum negative shaft power. The experimental data has an uncertainty of 3–4% up to $r/R \leq 0.8$ as compared to the mean value, as indicated by the shaded blue area around the solid-blue line (see Fig. 13a).

The LB-VLES$_{y^+\leq 10}$ exhibits good agreement with the experiment up to $r/R = 0.70$, with a maximum difference of 6% compared to the experimental mean values. However, further outboard, the LB-VLES$_{y^+\leq 10}$ predicts a 12% lower total pressure coefficient at $r/R = 0.80$ than the experimental mean value. However, the LB-VLES$_{y^+\leq 10}$ fails to predict the strong gradients in the outboard region for $r/R > 0.80$. Conversely, the LB-VLES$_{y^+\geq 15}$ captures the radial gradients of the total pressure coefficient but underestimates its magnitude by up to 21% for $r/R \leq 0.90$. This is consistent with the observed underprediction of $|C_T|$ for this operational condition in Fig. 7a. This underprediction is attributed to an inaccurate separation bubble size observed previously in Figs. 10 and 11.

The SRANS and URANS simulations show a good agreement with experimental data up to $r/R = 0.70$, with a maximum difference of 5% as compared to the experimental mean values. Similar to the LB-VLES$_{y^+\leq 10}$, the RANS simulations also fail to predict the strong gradients at higher radial coordinates, resulting in a 15% lower total pressure coefficient at $r/R = 0.80$ as compared to the experimental mean values (see Fig. 13a). Though the BEM and LL theories capture the radial gradients of the total pressure coefficient up to $r/R \leq 0.8$, the absolute values significantly diverge from the experimental data, underestimating the total pressure coefficient by up to 30% and 23% for $r/R \leq 0.8$. This is in agreement with the previously seen discrepancies in the normal-force coefficient in Table 9.

Figure 13b compares the thrust distributions obtained from the different numerical methods for $J = 1.10$. As expected, similar differences are present in the thrust distribution as observed in the total pressure coefficient profiles in Fig. 13a. Besides the radial location and amplitude of the loading peak (based on Fig. 13a), the LB-VLES$_{y^+\leq 10}$ is deemed to represent the thrust distribution well. Therefore, LB-VLES$_{y^+\leq 10}$ has been used as the reference for comparing power distribution along the blade span in Fig. 13c.

The BEM and LL methods predict a considerably different power distribution from the LB-VLES$_{y^+\leq 10}$. These methods underpredict the power distribution in the inboard part of the blade by 20–30% and overpredict the power distribution in the outboard part of the blade ($r/R \geq 0.60$) by more than 40% as compared to the LB-VLES$_{y^+\leq 10}$. The SRANS and URANS simulations have a power distribution similar to the LB-VLES$_{y^+\leq 10}$, except for the 6% overprediction of power peak by the former compared to the latter. The LB-VLES$_{y^+\geq 15}$ has a similar distribution as the LB-VLES$_{y^+\leq 10}$ for the inboard part of the blade ($r/R \leq 0.60$) with a difference of less than 10% up to $r/R \leq 0.60$. However, the LB-VLES$_{y^+\geq 15}$ significantly overpredicts the power distribution in the outboard part of the blade (more than 30%), resulting in a 16% higher integrated power than LB-VLES$_{y^+\leq 10}$, as observed in Table 7.

Lastly, blade loading comparisons were conducted for $J = 1.48$, representing the highest advance ratio considered in this paper. As the experimental total pressure coefficient profile is unavailable for this condition, only the thrust and power distributions have been compared between different numerical methods (see Fig. 14). Given the good match between the experimental data and URANS simulations in integrated performance in Fig. 7, and in the absence of other pertinent data, URANS simulations are considered the reference for comparing blade loading distributions.

Compared to higher-fidelity simulations, BEM and LL predict completely different loading distributions in Fig. 14. As mentioned before, these deviations may not be solely due to inaccuracies in polar data; they might be rooted in the breakdown of underlying assumptions inherent to these methods due to extensive flow separation. Though SRANS and URANS have an identical solution in all the previous results, some differences can be observed between the two for $J = 1.48$ in Fig. 14. These variations underline the increasing significance of unsteadiness with the increase in advance ratio due to the increase in flow separation. In contrast to the results seen in Fig. 13 for $J = 1.10$, LB-VLESs$_{y^+\geq 15}$ for $J = 1.48$ predict similar radial gradients as URANS simulations for both thrust and power distributions. This shows that fully separated flow is comparatively easier to simulate using wall models than flows with reattachment zones. Consequently, it strengthens the argument that the LB-VLESs$_{y^+\geq 15}$ are suitable for capturing the general trend of the propeller performance in negative thrust conditions.

D. Phase-Locked Flowfield in the Propeller Slipstream

In this section, the nondimensional phase-locked in-plane vorticity (ω_t^*) component has been compared in the propeller slipstream. The

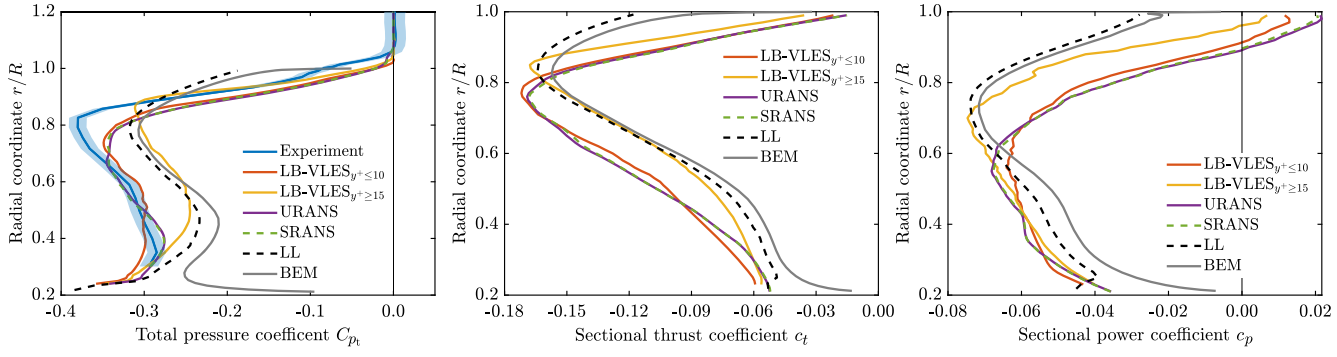

a) Total pressure coefficient **b) Thrust distribution** **c) Power distribution**

Fig. 13 Total pressure coefficient C_{p_t} at $0.15R$ downstream of propeller center and blade loading at a negative thrust condition ($J = 1.10$) near the maximum power output point.

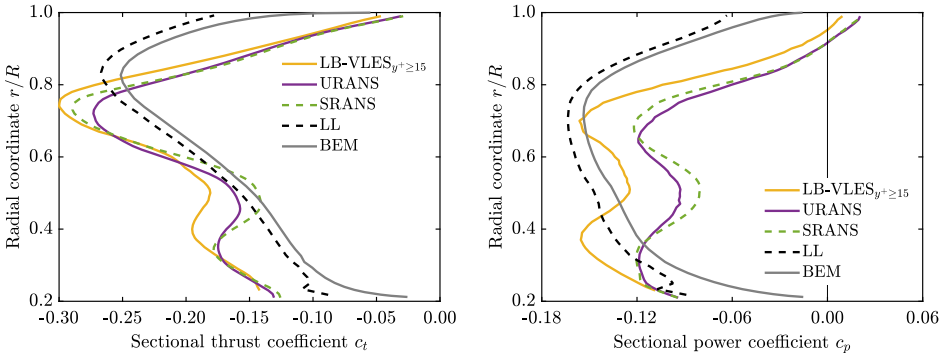

a) Thrust distribution **b) Power distribution**

Fig. 14 Comparison of blade loading at a negative thrust condition with fully separated flow ($J = 1.48$).

purpose of comparing ω_t^* is twofold. Firstly, to assess the efficacy of various simulations in preserving the wake structure in the slipstream, given the current mesh and computational cost. Secondly, to evaluate the sensitivity of the wake structure to discrepancies observed in blade loadings in the preceding section. These aspects hold significant relevance for future investigations related to propeller–wing interactions. The same advance ratios have been considered in this section as before: $J = 0.60$ (positive thrust) and 1.10 (negative thrust). Due to a similar flowfield in SRANS and URANS simulations, this section excludes URANS simulations to maintain brevity.

1. *Positive Thrust Condition ($J = 0.60$)*

Figure 15 compares the phase-locked nondimensional in-plane vorticity component in the propeller slipstream for the positive thrust condition ($J = 0.60$). The figure depicts two distinct wake structures, which will be referred to as the upstream and downstream wake structures in the following discussion.

The LB-VLES$_{y^+\leq 10}$ shows blade-wake and tip-vortex structures similar to the experiment. The negative in-plane vorticity region of the upstream wake around $r/R \approx 1.0$ extends up to $0.97R$ in the LB-VLES$_{y^+\leq 10}$ as compared to up to $0.95R$ in the experiment, which agrees with the differences previously observed in the radial distribution of total pressure in Fig. 12a. Also, the region with positive vorticity in the downstream wake structure extends up to $0.95R$ as compared to $0.90R$ in the experiment. This is the consequence of the underprediction of the blade loading peak, resulting in decreased slipstream contraction in the LB-VLES$_{y^+\leq 10}$. Nevertheless, the blade wakes from the inboard part of the blade in the LB-VLES$_{y^+\leq 10}$ agree well with the experimental data.

The LB-VLESs$_{y^+\geq 15}$ have a similar mesh in the propeller slipstream as LB-VLESs$_{y^+\leq 10}$. Though both have similar blade-wake and tip-vortex structures, some differences can be noticed upon careful observation (see Figs. 15b and 15c). The most significant difference is the presence of the secondary vortices around the blade-wake and tip-vortex structures in the LB-VLES$_{y^+\geq 15}$, which are absent in the LB-VLES$_{y^+\leq 10}$. The secondary vortices are expected to be the result of different blade loading and flow features around the propeller blades in the LB-VLES$_{y^+\geq 15}$ as compared to the LB-VLES$_{y^+\leq 10}$ as seen in the preceding sections.

The SRANS simulation shows diffused tip and root vortex regions at locations broadly consistent with the experiment (see Fig. 15d). The diffusion of blade wake and tip vortex in SRANS simulations is expected to be a consequence of two factors: the relatively coarse mesh in the propeller wake in RANS simulations as compared to LB-VLES simulations and the inherently higher numerical diffusion characteristic of RANS simulations compared to LB-VLES simulations [49,50]. It should be noted that the current RANS mesh was not set up for maximum preservation of the wake

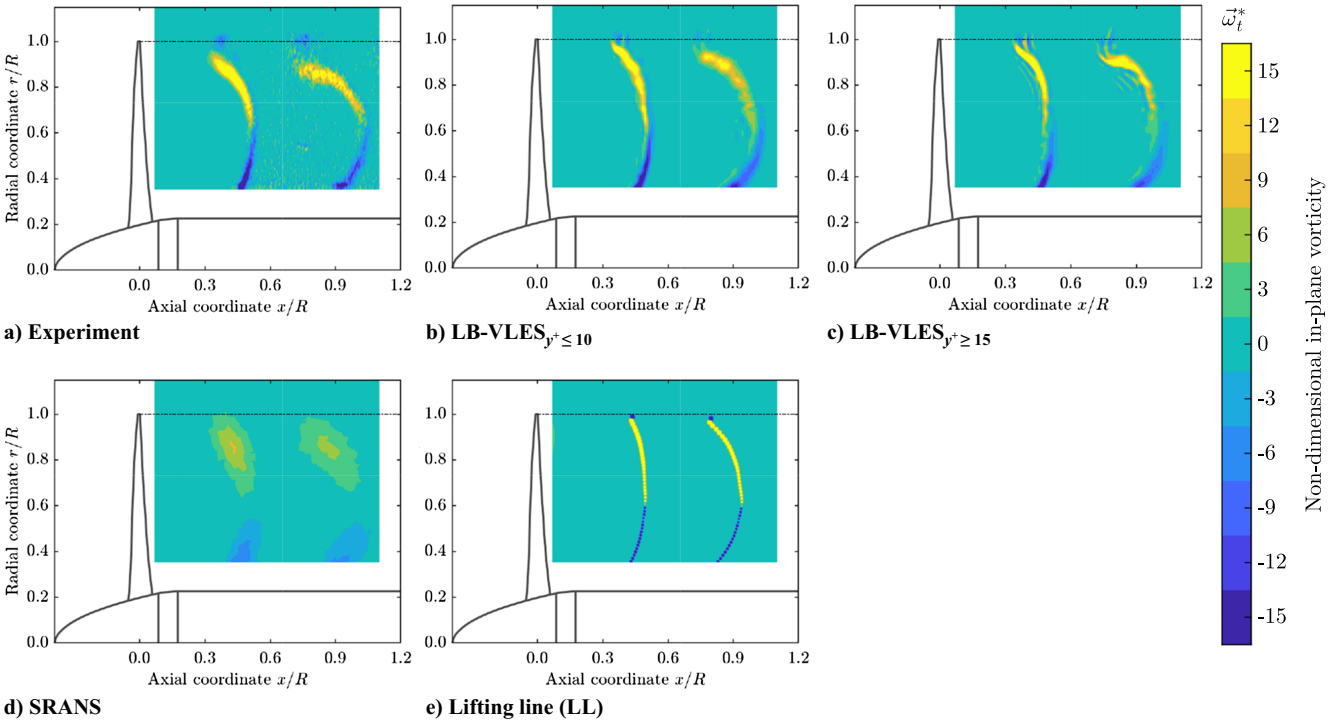

a) Experiment **b) LB-VLES$_{y^+\leq 10}$** **c) LB-VLES$_{y^+\geq 15}$**

d) SRANS **e) Lifting line (LL)**

Fig. 15 Comparison of phase-locked nondimensional in-plane vorticity component ω_t^* at the positive thrust condition ($J = 0.60$).

Downloaded by Technische Universiteit Delft on October 7, 2024 | http://arc.aiaa.org | DOI: 10.2514/1.J064093

Downloaded by Technische Universiteit Delft on October 7, 2024 | http://arc.aiaa.org | DOI: 10.2514/1.J064093

structures, and better results may be achievable with a focus on wake preservation with a similar computational cost.

Finally, Fig. 15e presents the vorticity distribution in the slipstream as obtained from LL using the slipstream contraction model [Eq. (1)]. Though qualitatively LL shows somewhat similar wake structures as the experiment, quantitatively significant differences are present. The upstream tip vortex cuts the plane around $x/R = 0.43$ in the LL slipstream as compared to $x/R = 0.38$ in the experiment. Similarly, the second tip vortex passes through the plane at $x/R = 0.8$ in the LL slipstream as compared to $x/R = 0.75$ in the experiment. The differences in the location of the blade wake between LL and experimental slipstreams increase from the upstream wake to the downstream wake due to the lower axial slipstream velocity in the former. For instance, at $r/R = 0.5$, the blade wakes in the LL flowfield are located at $x/R = 0.48$ and 0.92 as compared to $x/R = 0.51$ and 1.02 in the experimental flowfield. This suggests a lower convection velocity of the wake structures in LL than in the experiment, despite the higher total pressure coefficient in the former (see Fig. 12a). These discrepancies can be partially attributed to the absence of the nacelle in the LL simulation and partially to the assumptions made in the slipstream contraction model. Despite this, considering the substantially lower computational cost of the LL method as compared to other numerical methods, the LL method provides a valuable first approximation of the slipstream vorticity distribution in the wake.

2. *Negative Thrust Condition ($J = 1.10$)*

Figure 16 compares the nondimensional in-plane vorticity component for the negative thrust condition, i.e., $J = 1.10$. Again, the LB-VLES$_{y^+\leq 10}$ shows a wake structure similar to the experiment at approximately the same location (see Figs. 16a and 16b). However, the tip-vortex shape in the LB-VLES$_{y^+\leq 10}$ is slightly different than in the experiment.

The LB-VLES$_{y^+\geq 15}$ in Fig. 16c predicts the blade-wake structure to be comparatively more concentrated and well-defined, which could be attributed to the underpredicted flow separation, as shown in Fig. 10c. The overall wake structure and tip vortex shape are somewhat similar to the experiment, as expected from Fig. 13a, given the good agreement between the LB-VLES$_{y^+\geq 15}$ and experiment in terms of radial gradients.

In the case of the SRANS simulations, a diffused region of tip vortex and blade wake can be observed approximately at the same location as the experiment (see Fig. 16d). However, further insights are hindered by the numerical diffusion inherent in SRANS simulations. Examining the LL slipstream in Fig. 16e, a well-defined tip vortex and blade wake structure are evident, with the blade wake and tip vortex located at approximately the same location as the experimental flowfield. Notably, while providing a reasonable initial estimate of the vorticity distribution in the wake, the LL model does not capture the diffusion and dissipation of wake structures due to the absence of viscous losses and wake mixing.

V. Conclusions

This study systematically evaluated various numerical methods for modeling the aerodynamic performance of propellers across both positive and negative thrust regimes. The findings from this study provide valuable guidance for researchers seeking the optimal approach for investigating propeller performance across a diverse range of operating conditions, depending on the desired accuracy.

The comparison of integrated performance (C_T and C_P) showed that BEM and LL can predict the trends of propeller performance in the positive thrust regime, though with an offset, for instance, an offset of 7–11% at $J = 0.60$ for the propeller and pitch setting considered in this paper. The total pressure distribution in the slipstream also shows reasonable agreement with experimental data (overestimating the peak by 5–6%). Despite the differences, BEM and LL methods combined with RFOIL offer qualitatively reasonable chordwise pressure distributions at positive thrust.

In the negative thrust conditions, while BEM and LL initially follow experimental trends in thrust and power up to the maximum power output point ($J = 1.10$ in this study), they quickly diverge from experiments for higher advance ratios, underestimating thrust magnitude, and significantly overestimating power magnitude (by more than 25% at $J = 1.48$). This is a consequence of the fact that the blade loading distributions derived from BEM and LL theories cease to be representative of the actual expected distribution as per higher-fidelity simulations.

Therefore, while BEM and LL theories are suitable for predicting general trends and optimizing propeller performance in positive thrust conditions, their applicability in the negative thrust regime is

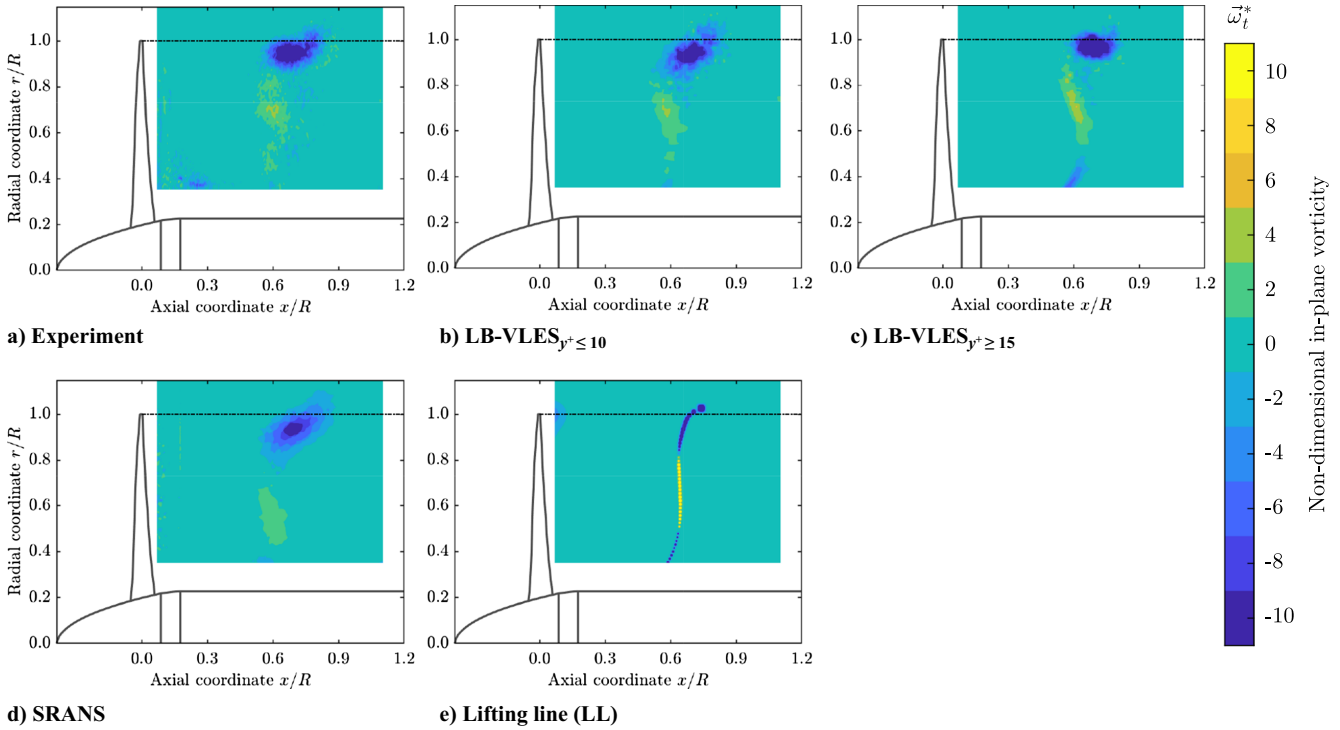

Fig. 16 Comparison of phase-locked nondimensional in-plane vorticity component ω_t^* at the negative thrust condition ($J = 1.10$).

limited to conditions without significant flow separation around the blades. In this study, this limitation manifested before the maximum power output point. The inaccuracies in performance prediction by BEM and LL are suspected to arise not just from polar data limitations but also from the breakdown of the inherent assumption of 2D flow in these methods. Further research is needed to thoroughly explore and validate these assumptions in the negative thrust regime.

Besides the propeller performance prediction, the vorticity distribution in the propeller wake calculated using LL theory provided a good first approximation for both positive and negative thrust conditions (up to the maximum power output point) and, therefore, can be a useful tool for propeller–wing interaction studies.

The SRANS and URANS simulations showcase near-identical solutions across almost the entire range of advance ratios. At the positive thrust condition ($J = 0.60$), the errors in C_T and C_P range from 3–4% and 7–8%, respectively, with an 11% underprediction of the total pressure peak in the slipstream compared to the experiment. On the contrary, these errors decrease to 1–2% in C_T and less than 1% in C_P at the negative thrust condition ($J = 1.10$). The difference between RANS simulations and experimental data increases with the advance ratio in the negative thrust regime, reaching a 3% error in C_T for URANS simulations at $J = 1.48$ due to the error introduced by the turbulence modeling in predicting separated flows. Also, the differences between the SRANS and URANS become apparent in this condition due to the increasing influence of unsteadiness induced by the separated flow.

While RANS simulations offer a viable choice for comprehensively studying propeller performance within both positive and negative thrust regimes, it is essential to note that the blade wake and tip vortex structures tend to diffuse rapidly in RANS-simulated cases. This diffusion results from the coarser mesh resolution and comparatively higher numerical diffusion in RANS simulations than in LB-VLES simulations. Therefore, while RANS simulations are suitable for predicting propeller performance, their use for capturing phase-locked slipstream data requires refinement of the mesh beyond the point required for predicting integrated performance.

The comparison of LB-VLES simulations with experimental data highlights the crucial role of using $y^+ \leq 10$ for accurate solutions, particularly in negative thrust conditions. The LB-VLES$_{y^+\leq 10}$ align well with experimental data (error <1% at $J = 1.10$), albeit with significantly increased computational resources (over 30 times compared to LB-VLES$_{y^+\geq 15}$). In contrast, though the computation cost of the LB-VLES$_{y^+\geq 15}$ is similar to URANS simulations, the LB-VLES$_{y^+\geq 15}$ overestimates the power magnitude by 16% when compared to experimental data at $J = 1.10$ (close to the maximum power output point). This disparity primarily arises from inaccuracies in modeling reattachment locations along the blade span. Despite the errors in absolute values, LB-VLES$_{y^+\geq 15}$ offer an alternative option for capturing the general trend of propeller performance. Both types of LB-VLES simulations effectively preserve propeller wake structures due to their inherent lower numerical diffusion and lower computational cost per mesh element compared to RANS simulations. This characteristic could be useful for propeller–wing interaction studies.

Ultimately, the most suitable numerical method depends on the specific research objectives and available resources. BEM and LL theories are good tools for predicting general trends in propeller performance and optimization in the positive thrust regime. However, these methods should be used with caution in the negative thrust regime. LL theory provides a good first estimation of the phase-locked propeller slipstream and can be useful for studies interested in accounting for propeller–wing interactions in aircraft design studies. Both SRANS and URANS simulations with $y^+ < 1$ provide a good balance between accuracy and computational cost for propeller performance studies in both positive and negative thrust regimes. However, special attention is needed while meshing for the preservation of tip-vortex and blade wake structures in the propeller slipstream. LB-VLES$_{y^+\geq 15}$ can be used as an alternative for studies interested in propeller–wing interactions due to their reduced numerical diffusion and competitive computational cost compared to URANS simulations. However, one must be cautious of errors introduced by wall modeling in LB-VLES$_{y^+\geq 15}$. Though LB-VLES$_{y^+\leq 10}$ provide excellent agreement with the experiments in negative thrust conditions, this accuracy comes at a tremendous computational cost (over 30 times LB-VLES$_{y^+\geq 15}$) and may not be practical.

These findings highlight the importance of carefully selecting a numerical method based on specific research objectives and computational resources. Future experiments focused on measuring surface quantities such as skin friction and pressure distribution could provide valuable insight into flow separation, further enhancing the assessment of the accuracy of numerical models.

Acknowledgments

The research leading to these results is part of the FUTPRINT50 project. This project has received funding from the European Union's Horizon 2020 Research and Innovation program under Grant Agreement No. 875551. This work made use of the Dutch national e-infrastructure with the support of the SURF Cooperative using Grant No. EINF-2733 and EINF-6911. The authors would like to thank Robert Nederlof for providing the experimental data for the validation of the simulations.

References

[1] Hepperle, M., "Electric Flight—Potential and Limitations," *Energy Efficient Technologies and Concepts of Operation*, NATO Science and Technology Organization, Lisbon, Portugal, 2012, https://elib.dlr.de/78726/.

[2] Kim, H. D., "Distributed Propulsion Vehicles," *27th International Congress of the Aeronautical Sciences*, Nice, France, Paper ICAS 2010-1.1.3, 2010, https://ntrs.nasa.gov/api/citations/20100036222/downloads/20100036222.pdf.

[3] Sinnige, T., van Arnhem, N., Stokkermans, T. C., Eitelberg, G., and Veldhuis, L. L., "Wingtip-Mounted Propellers: Aerodynamic Analysis of Interaction Effects and Comparison with Conventional Layout," *Journal of Aircraft*, Vol. 56, No. 1, 2019, pp. 295–312. https://doi.org/10.2514/1.C034978

[4] Hartman, E. P., "Negative Thrust and Torque Characteristics of an Adjustable-Pitch Metal Propeller," Annual Report-National Advisory Committee for Aeronautics, Vol. 19, 1933, p. 421, http://hdl.handle.net/2060/19930091538.

[5] Hedrick, W. S., and Douglass, W. M., "An Experimental Investigation of the Thrust and Torque Produced by Propellers Used as Aerodynamic Brakes," NACA WR-A-27, 1944, http://hdl.handle.net/2060/19930093338.

[6] Thomas, J. L., and Hansman, R. J., "Community Noise Reduction Assessment of Using Windmilling Drag on Approach by Hybrid Electric Aircraft," *AIAA Aviation 2020 Forum*, AIAA Paper 2020-2877, June 2020. https://doi.org/10.2514/6.2020-2877

[7] Eržen, D., Andrejašič, M., Lapuh, R., Tomažič, J., Gorup, Č., and Kosel, T., "An Optimal Propeller Design for In-Flight Power Recuperation on an Electric Aircraft," *2018 Aviation Technology, Integration, and Operations Conference*, AIAA Paper 2018-3206, June 2018. https://doi.org/10.2514/6.2018-3206

[8] Sinnige, T., Stokkermans, T. C. A., van Arnhem, N., and Veldhuis, L. L. M., "Aerodynamic Performance of a Wingtip-Mounted Tractor Propeller Configuration in Windmilling and Energy-Harvesting Conditions," *AIAA Aviation 2019 Forum*, AIAA Paper 2019-3033, June 2019. https://doi.org/10.2514/6.2019-3033

[9] Gunnarsson, G., Skúlason, J. B., Sigurbjarnarson, A., and Enge, S., "Regenerative Electric/Hybrid Drive Train for Ships," Nordic Innovation Publication 2016:02, Jan. 2016, https://norden.diva-portal.org/smash/get/diva2:1294665/FULLTEXT01.pdf.

[10] Nodama, T., and Sunada, S., "Puropera ni yoru batteri jūden ni kansuru kentō," *Proceedings of the Japan Society for Aeronautics and Astronautics*, Vol. 63, No. 1, 2015, pp. 8–12; also A Study on Battery Charging by Propellers (in English). https://doi.org/10.2322/jjsass.63.8

[11] Nederlof, R., Ragni, D., and Sinnige, T., "Experimental Investigation of the Aerodynamic Performance of a Propeller at Positive and Negative Thrust and Power," *AIAA Aviation 2022 Forum*, AIAA Paper 2022-3893, June 2022. https://doi.org/10.2514/6.2022-3893

[12] Goyal, J., Sinnige, T., Avallone, F., and Ferreira, C., "Aerodynamic and Aeroacoustic Characteristics of an Isolated Propeller at Positive and Negative Thrust," *AIAA Aviation 2021 Forum*, AIAA Paper 2021-2187, June 2021. https://doi.org/10.2514/6.2021-2187

[13] Goyal, J., Sinnige, T., Ferreira, C. S., and Avallone, F., "Aerodynamics and Far-Field Noise Emissions of a Propeller in Positive and Negative

Downloaded by Technische Universiteit Delft on October 7, 2024 | http://arc.aiaa.org | DOI: 10.2514/1.J064093

Thrust Regimes at Non-Zero Angles of Attack," *AIAA Aviation 2023 Forum*, AIAA Paper 2023-3217, June 2023. https://doi.org/10.2514/6.2023-3217

[14] Barlow, J., Rae, W., and Pope, A., *Low-Speed Wind Tunnel Testing*, Wiley, New York, 1999, https://books.google.co.in/books?id=nUHWDwAAQBAJ.

[15] Rwigema, M. K., "Propeller Blade Element Momentum Theory with Vortex Wake Deflection," *27th International Congress of the Aeronautical Sciences*, ICAS Paper 2010-2.3.3, Nice, France, 2010, http://www.icas.org/ICAS_ARCHIVE/ICAS2010/PAPERS/434.PDF.

[16] Burton, T., Sharpe, D., Jenkins, N., and Bossanyi, E., *Wind Energy Handbook*, Vol. 2, Wiley Online Library, Hoboken, NJ, 2001. https://doi.org/10.1002/9781119992714

[17] van Rooij, R., "Modification of the Boundary Layer Calculation in RFOIL for Improved Airfoil Stall Prediction," Rept. IW-96087R, Delft Univ. of Technology, Delft, The Netherlands, Sept. 1996, https://www.osti.gov/etdeweb/biblio/20102159.

[18] Drela, M., "XFOIL: An Analysis and Design System for Low Reynolds Number Airfoils," *Low Reynolds Number Aerodynamics*, edited by T. J. Mueller, Springer–Verlag, Berlin, 1989, pp. 1–12. https://doi.org/10.1007/978-3-642-84010-4_1

[19] Yu, W., Zhang, M. M., and Xu, J. Z., "Effect of Smart Rotor Control Using a Deformable Trailing Edge Flap on Load Reduction Under Normal and Extreme Turbulence," *Energies*, Vol. 5, No. 9, 2012, pp. 3608–3626. https://doi.org/10.3390/en5093608

[20] Snel, H., Houwink, R., and Bosschers, J., "Sectional Prediction of Lift Coefficients on Rotating Wind Turbine Blades in Stall," Rept. ECN-93-052, Energy Research Center of the Netherlands, Petten, The Netherlands, 1993, https://www.osti.gov/etdeweb/biblio/6693027.

[21] Bosschers, J., Montgomerie, B., Brand, A., and van Rooij, R., "Influence of Blade Rotation on the Sectional Aerodynamics of Rotational Blades," *22nd European Rotorcraft Forum*, Brighton, U.K., Paper ERF-1996-Vol1-53, 1996, http://hdl.handle.net/20.500.11881/3167.

[22] Goyal, J., "Blade Element Momentum Theory for Positive and Negative Thrust Propellers," 4TU.ResearchData.Software, 2024. https://doi.org/10.4121/e748a68d-5f15-4757-b904-880bcec8217b

[23] Prandtl, L., and Betz, A., "Vier abhandlungen zur hydrodynamik und aerodynamik," Göttinger Nachr, Göttingen, Germany, 1927, https://univerlag.uni-goettingen.de/bitstream/handle/3/isbn-978-3-941875-75-3/GKSM3.pdf?sequence=1&isAllowed=y.

[24] Katz, J., and Plotkin, A., *Low-Speed Aerodynamics*, Vol. 13, Cambridge Univ. Press, Cambridge, England, U.K., 2001. https://doi.org/10.1017/CBO9780511810329

[25] Veldhuis, L. L. M., "Propeller Wing Aerodynamic Interference," Ph.D. Dissertation, Delft Univ. of Technology, Delft, The Netherlands, 2005, http://resolver.tudelft.nl/uuid:8ffbde9c-b483-40de-90e0-97095202fbe3.

[26] Anon., *ANSYS® Academic Research Release 2019 R3 Help System, Fluent*, ANSYS, Inc., Canonsburg, PA, 2019.

[27] Stokkermans, T. C. A., van Arnhem, N., Sinnige, T., and Veldhuis, L. L. M., "Validation and Comparison of RANS Propeller Modeling Methods for Tip-Mounted Applications," *AIAA Journal*, Vol. 57, No. 2, 2019, pp. 566–580. https://doi.org/10.2514/1.J057398

[28] van Arnhem, N., Vos, R., and Veldhuis, L. L. M., "Aerodynamic Loads on an Aft-Mounted Propeller Induced by the Wing Wake," *AIAA Scitech 2019 Forum*, AIAA Paper 2019-1093, Jan. 2019. https://doi.org/10.2514/6.2019-1093

[29] Spalart, P. R., and Allmaras, S. R., "A One-Equation Turbulence Model for Aerodynamic Flows," *30th Aerospace Sciences Meeting*, AIAA Paper 1992-0439, June 1992. https://doi.org/10.2514/6.1992-439

[30] Dacles-Mariani, J., Zilliac, G. G., Chow, J. S., and Bradshaw, P., "Numerical/Experimental Study of a Wingtip Vortex in the Near Field," *AIAA Journal*, Vol. 33, No. 9, 1995, pp. 1561–1568. https://doi.org/10.2514/3.12826

[31] Roache, P. J., "Quantification of Uncertainty in Computational Fluid Dynamics," *Annual Review of Fluid Mechanics*, Vol. 29, No. 1, 1997, pp. 123–160. https://doi.org/10.1146/annurev.fluid.29.1.123

[32] Eça, L., and Hoekstra, M., "Discretization Uncertainty Estimation Based on a Least Squares Version of the Grid Convergence Index," *Proceedings of the 2nd Workshop on CFD Uncertainty Analysis*, 2006, https://maretec.tecnico.ulisboa.pt/html_files/CFD_workshops/html_files_2006/papers/paper_istmarin.pdf.

[33] Succi, S., *The Lattice Boltzmann Equation: For Fluid Dynamics and Beyond*, Oxford Univ. Press, Oxford, 2001. https://doi.org/10.1063/1.1537916

[34] Shan, X., Yuan, X.-F., and Chen, H., "Kinetic Theory Representation of Hydrodynamics: A Way Beyond the Navier–Stokes Equation," *Journal of Fluid Mechanics*, Vol. 550, March 2006, pp. 413–441. https://doi.org/10.1017/S0022112005008153

[35] Casalino, D., Romani, G., Zhang, R., and Chen, H., "Lattice-Boltzmann Calculations of Rotor Aeroacoustics in Transitional Boundary Layer Regime," *Aerospace Science and Technology*, Vol. 130, Nov. 2022, Paper 107953. https://doi.org/10.1016/j.ast.2022.107953

[36] Chen, H., Zhang, R., and Gopalakrishnan, P., "Lattice Boltzmann Collision Operators Enforcing Isotropy and Galilean Invariance," Feb. 2017, https://patents.google.com/patent/CA2919062A1/en.

[37] Chen, H., Chen, S., and Matthaeus, W. H., "Recovery of the Navier-Stokes Equations Using a Lattice-Gas Boltzmann Method," *Physical Review A*, Vol. 45, No. 8, 1992, Paper R5339. https://doi.org/10.1103/PhysRevA.45.R5339

[38] Yakhot, V., and Orszag, S. A., "Renormalization Group Analysis of Turbulence. I. Basic Theory," *Journal of Scientific Computing*, Vol. 1, No. 1, 1986, pp. 3–51. https://doi.org/10.1007/BF01061452

[39] Teixeira, C. M., "Incorporating Turbulence Models into the Lattice-Boltzmann Method," *International Journal of Modern Physics C*, Vol. 9, No. 8, 1998, pp. 1159–1175. https://doi.org/10.1142/S0129183198001060

[40] Wilcox, D., *Turbulence Modeling for CFD*, Vol. 1, DCW Industries, La Canada, CA, 2006, pp. 103–217, https://books.google.co.in/books?id=tFNNPgAACAAJ.

[41] Launder, B. E., and Spalding, D. B., "The Numerical Computation of Turbulent Flows," *Numerical Prediction of Flow, Heat Transfer, Turbulence and Combustion*, Elsevier, New York, 1983, pp. 96–116. https://doi.org/10.1016/B978-0-08-030937-8.50016-7

[42] Avallone, F., van den Ende, L., Li, Q., Ragni, D., Casalino, D., Eitelberg, G., and Veldhuis, L., "Aerodynamic and Aeroacoustic Effects of Swirl Recovery Vanes Length," *Journal of Aircraft*, Vol. 56, No. 6, 2019, pp. 2223–2235. https://doi.org/10.2514/1.C035552

[43] Goyal, J., Avallone, F., and Sinnige, T., "Isolated Propeller Aeroacoustics at Positive and Negative Thrust," *Aerospace Science and Technology*, Vol. 147, March 2024, Paper 109021. https://doi.org/10.1016/j.ast.2024.109021

[44] Himmelskamp, H., Aerodynamische Versuchsanstalt Göttingen, Great Britain. Ministry of Aircraft Production, and Luftfahrtforschungsanstalt Hermann Georing, "Profile Investigations on a Rotating Airscrew," ARC-10856, Ministry of Aircraft Production, 1947, https://books.google.co.in/books?id=VlK3tgAACAAJ.

[45] O'meara, M., and Mueller, T. J., "Laminar Separation Bubble Characteristics on an Airfoil at Low Reynolds Numbers," *AIAA Journal*, Vol. 25, No. 8, 1987, pp. 1033–1041. https://doi.org/10.2514/3.9739

[46] Ol, M., McCauliffe, B., Hanff, E., Scholz, U., and Kähler, C., "Comparison of Laminar Separation Bubble Measurements on a Low Reynolds Number Airfoil in Three Facilities," *35th AIAA Fluid Dynamics Conference and Exhibit*, AIAA Paper 2005-5149, 2005. https://doi.org/10.2514/6.2005-5149

[47] Temmerman, L., and Leschziner, M. A., "Large Eddy Simulation of Separated Flow in a Streamwise Periodic Channel Constriction," *2nd Symposium on Turbulence and Shear Flow Phenomena*, Begel House, Inc., Danbury, CT, 2001, pp. 399–404. https://doi.org/10.1615/TSFP2.2300

[48] Temmerman, L., Leschziner, M. A., Mellen, C. P., and Fröhlich, J., "Investigation of Wall-Function Approximations and Subgrid-Scale Models in Large Eddy Simulation of Separated Flow in a Channel with Streamwise Periodic Constrictions," *International Journal of Heat and Fluid Flow*, Vol. 24, No. 2, 2003, pp. 157–180. https://doi.org/10.1016/S0142-727X(02)00222-9

[49] Bres, G., Pérot, F., and Freed, D., "Properties of the Lattice Boltzmann Method for Acoustics," *15th AIAA/CEAS Aeroacoustics Conference (30th AIAA Aeroacoustics Conference)*, AIAA Paper 2009-3395, 2009. https://doi.org/10.2514/6.2009-3395

[50] Marié, S., Ricot, D., and Sagaut, P., "Comparison Between Lattice Boltzmann Method and Navier–Stokes High Order Schemes for Computational Aeroacoustics," *Journal of Computational Physics*, Vol. 228, No. 4, 2009, pp. 1056–1070. https://doi.org/10.1016/j.jcp.2008.10.021

F. N. Coton
Associate Editor

Downloaded by Technische Universiteit Delft on October 7, 2024 | http://arc.aiaa.org | DOI: 10.2514/1.J064093